



University of Kentucky  
UKnowledge

---

Theses and Dissertations--Computer Science

Computer Science

---

2014

## Nuclei/Cell Detection in Microscopic Skeletal Muscle Fiber Images and Histopathological Brain Tumor Images Using Sparse Optimizations

Hai Su

University of Kentucky, [hai.su@uky.edu](mailto:hai.su@uky.edu)

[Right click to open a feedback form in a new tab to let us know how this document benefits you.](#)

---

### Recommended Citation

Su, Hai, "Nuclei/Cell Detection in Microscopic Skeletal Muscle Fiber Images and Histopathological Brain Tumor Images Using Sparse Optimizations" (2014). *Theses and Dissertations--Computer Science*. 24. [https://uknowledge.uky.edu/cs\\_etds/24](https://uknowledge.uky.edu/cs_etds/24)

This Master's Thesis is brought to you for free and open access by the Computer Science at UKnowledge. It has been accepted for inclusion in Theses and Dissertations--Computer Science by an authorized administrator of UKnowledge. For more information, please contact [UKnowledge@lsv.uky.edu](mailto:UKnowledge@lsv.uky.edu).

## STUDENT AGREEMENT:

I represent that my thesis or dissertation and abstract are my original work. Proper attribution has been given to all outside sources. I understand that I am solely responsible for obtaining any needed copyright permissions. I have obtained needed written permission statement(s) from the owner(s) of each third-party copyrighted matter to be included in my work, allowing electronic distribution (if such use is not permitted by the fair use doctrine) which will be submitted to UKnowledge as Additional File.

I hereby grant to The University of Kentucky and its agents the irrevocable, non-exclusive, and royalty-free license to archive and make accessible my work in whole or in part in all forms of media, now or hereafter known. I agree that the document mentioned above may be made available immediately for worldwide access unless an embargo applies.

I retain all other ownership rights to the copyright of my work. I also retain the right to use in future works (such as articles or books) all or part of my work. I understand that I am free to register the copyright to my work.

## REVIEW, APPROVAL AND ACCEPTANCE

The document mentioned above has been reviewed and accepted by the student's advisor, on behalf of the advisory committee, and by the Director of Graduate Studies (DGS), on behalf of the program; we verify that this is the final, approved version of the student's thesis including all changes required by the advisory committee. The undersigned agree to abide by the statements above.

Hai Su, Student

Dr. Jinze Liu, Major Professor

Dr. Miroslaw Truszczynski, Director of Graduate Studies

Nuclei/Cell Detection in Microscopic Skeletal Muscle Fiber Images and  
Histopathological Brain Tumor Images Using Sparse Optimizations

---

THESIS

---

A thesis submitted in partial  
fulfillment of the requirements for  
the degree of Master of Science in  
the College of Engineering at the  
University of Kentucky

By  
Hai Su  
Lexington, Kentucky

Director: Dr. Jinze Liu, Associate Professor of Computer Science  
Lexington, Kentucky  
Co-Director: Dr. Lin Yang, Associate Professor of J. Crayton Pruitt Family  
Department of Biomedical Engineering  
Gainesville, Florida 2014

Copyright© Hai Su 2014

## ABSTRACT OF THESIS

### Nuclei/Cell Detection in Microscopic Skeletal Muscle Fiber Images and Histopathological Brain Tumor Images Using Sparse Optimizations

Nuclei/Cell detection is usually a prerequisite procedure in many computer-aided biomedical image analysis tasks. In this thesis we propose two automatic nuclei/cell detection frameworks. One is for nuclei detection in skeletal muscle fiber images and the other is for brain tumor histopathological images.

For skeletal muscle fiber images, the major challenges include: i) shape and size variations of the nuclei, ii) overlapping nuclear clumps, and iii) a series of z-stack images with out-of-focus regions. We propose a novel automatic detection algorithm consisting of the following components: 1) The original z-stack images are first converted into one all-in-focus image. 2) A sufficient number of hypothetical ellipses are then generated for each nuclei contour. 3) Next, a set of representative training samples and discriminative features are selected by a two-stage sparse model. 4) A classifier is trained using the refined training data. 5) Final nuclei detection is obtained by mean-shift clustering based on inner distance. The proposed method was tested on a set of images containing over 1500 nuclei. The results outperform the current state-of-the-art approaches.

For brain tumor histopathological images, the major challenges are to handle significant variations in cell appearance and to split touching cells. The proposed novel automatic cell detection consists of: 1) Sparse reconstruction for splitting touching cells. 2) Adaptive dictionary learning for handling cell appearance variations. The proposed method was extensively tested on a data set with over 2000 cells. The result outperforms other state-of-the-art algorithms with  $F_1$  score = 0.96.

**KEYWORDS:** Nuclei/Cell Detection, Sparse Representation, Trivial Templates, Microscopic Images

Author's signature: \_\_\_\_\_ Hai Su

Date: \_\_\_\_\_ December 16, 2014

Nuclei/Cell Detection in Microscopic Skeletal Muscle Fiber Images and  
Histopathological Brain Tumor Images Using Sparse Optimizations

By  
Hai Su

Director of Thesis: Jinze Liu

Co-Director of Thesis: Lin Yang

Director of Graduate Studies: Miroslaw Truszczyński

Date: December 16, 2014

Dedicated to my lovely wife and daughter

## ACKNOWLEDGMENTS

I would like to express my special gratitude to my thesis advisor Dr. Jinze Liu and co-advisor Dr. Lin Yang who offered me inspiring guidance and support along all my research. I also would like to thank Dr. Ruigang Yang who served as my committee member. He provided me valuable insights and constructive criticism that contribute to the complete of this thesis. Thank them all for their time and efforts made for me towards my thesis defense.

I also appreciate the helps from Fuyong Xing, Fujun Liu, and Manish Sapkota, and Yuanpu Xie, who are my lab coworkers in Dr. Lin Yang's lab. Helps offered by them from time to time were involved in every step towards the complete of this thesis. Discussions with them helped me to avoid some vain endeavors. Source codes provided by them usually helped me to accelerate the progress.

Finally, I owe a lot of thanks to my dear wife Ji Liu and daughter Ivy Su. Their support is indispensable for the complete of my degree.

## TABLE OF CONTENTS

Acknowledgments . . . . .	iii
Table of Contents . . . . .	iv
List of Figures . . . . .	v
List of Tables . . . . .	vi
Chapter 1 Automatic Myonuclear Detection in Isolated Single Muscle Fibers . . . . .	1
1.1 Introduction . . . . .	1
1.2 Method . . . . .	2
1.3 Experimental Results . . . . .	11
Chapter 2 Nuclei Detection in Histopathological Brain Tumor Images . . . . .	21
2.1 Introduction . . . . .	21
2.2 Method . . . . .	23
2.3 Experimental Results . . . . .	30
Chapter 3 Conclusion and Future Work . . . . .	35
Bibliography . . . . .	36
Vita . . . . .	44



## LIST OF FIGURES

1.1	An all-in-focus image is synthesized from z-stack images. . . . .	2
1.2	An overview of the proposed algorithm. . . . .	3
1.3	(a) Original contour. (b) Concave point detection and refinement. . . . .	4
1.4	A demonstration of various ellipse fitting results. . . . .	5
1.5	Robust ellipse fitting using HEIV regression. . . . .	6
1.6	Examples to illustrate the <b>Set 3</b> features. . . . .	7
1.7	Examples to illustrate the <b>Set 4</b> features. . . . .	8
1.8	Mean-shift clustering based on inner distance. . . . .	10
1.9	An all-in-focus image (n) synthesized by multi-image fusion. . . . .	11
1.10	Examples showing effects of the geometric features. . . . .	12
1.11	The selected discriminative features by sparse representation. . . . .	13
1.12	The mean-shift clustering based on inner distance. . . . .	14
1.13	Detection results of nine randomly selected image patches. . . . .	14
1.14	The ROC curves using dictionary learning by K-selection v.s. BoW model. . . . .	15
1.15	Classification performance of four feature selection methods. . . . .	15
1.16	Comparison of the average AUCs using four feature selection methods. . . . .	16
1.17	Performance comparison with LoG [1], IRV [2], and SPV [3]. . . . .	17
2.1	An overview of the framework. . . . .	22
2.2	The local image structure is encoded by LSK. . . . .	24
2.3	Adaptive dictionary generation using two sample patches. . . . .	25
2.4	Reconstruction results and errors of four cells. . . . .	26
2.5	Sparse reconstruction with trivial template modeling the touching cells. . . . .	28
2.6	Probability maps and detection results. . . . .	29
2.7	Effect of the trivial templates. . . . .	30
2.8	Detection results of whole target images. . . . .	31
2.9	Qualitative comparison with LoG [1], IRV [2], and ITCN [4], and SPV [3]. . . . .	32
2.10	Effect of the number of local neighbors on the detection performance. . . . .	34

## LIST OF TABLES

1.1	A summary of the geometric features for learning based ellipse refinement.	19
1.2	The comparison of four feature Selection methods . . . . .	20
1.3	The pixel-wise seed detection accuracy compared with ground truth . . .	20
1.4	The comparative performance measured by precision and recall . . . . .	20
2.1	Comparative performance evaluation by seed offset. . . . .	33
2.2	Comparative performance evaluation for a circle with radius of 8 pixels .	33

# Chapter 1 Automatic Myonuclear Detection in Isolated Single Muscle Fibers

## 1.1 Introduction

Cell and organelle counting are fundamental measures in biological research. In the field of muscle biology, the number of nuclei is of particular interest given that muscle is organized as multinucleated myofibers, with each nucleus supporting a domain of cytoplasm. The ratio of myonuclei to cytoplasmic volume of the myofiber is termed the myonuclear domain. Contrary to dogma, recent evidence shows that the myonuclear domain is very flexible, changing during muscle growth, atrophy, and regeneration [5, 6]. The addition and subtraction of myonuclei to the existing myofiber presumably is the basis of skeletal muscle hypertrophy and atrophy. For example, myonuclei accretion usually increases during muscle hypertrophy, presumably through the fusion of muscle stem cells contributing myonuclei to the existing myofiber. Thus, accurate and efficient quantification of the number of myonuclei per fiber relative to fiber size, is an important factor to evaluate muscle adaptation, as well as its pathological conditions. Currently, manual counting is extremely time consuming and labor intensive. Computer assisted microscopic image analysis tools are better alternatives compared with manual quantifications with respect to efficiency.

There are many existing approaches for automatic cell or nuclear counting. The distance transform based method is commonly used to detect seeds in clustered objects. However, it does not work well for the tightly clustered or overlapping objects in which false positive error becomes non-negligible. Some algorithm improved the distance transform method by combining geometric and intensity information to provide more accurate detection [7, 8]. An algorithm [9] was proposed to filter out the false seeds by minimizing the false detections based on mutual proximity.

Watershed-based segmentation is a widely used method for splitting touching cells [10]. However, it suffers from over-segmentation. Various merging mechanisms based on hierarchical tree searching algorithm [11], anatomic characteristics of nuclei analysis [12], and topology dependence constraints [13] have been proposed. A cell segmentation algorithm using watershed-based cell splitting with photometric and shape information was proposed in [14]. A general segmentation framework for fluorescent images was proposed in [15]. The algorithm utilized both the image appearance information from both DNA and Actin channels. The inter-cellular interactions and the gradient information inside the cells were formulated as an energy functional, and minimized by a multiphase level set propagation. Watershed algorithms incorporating markers indicating object prior information were investigated in [16, 17, 18]. In [19], cell markers (used for marker controlled watershed) were detected by localizing the centers of the gravities in the cell clumps using kernel-based iterative radial voting. Jung *et al.* [20] developed a modified watershed algorithm using H-minima transform that integrates the shape information of nuclei. The H-value is derived by evaluating a shape distortion function to measure the fitting accuracy between the ellipse and nuclear contour. In [21], an adaptive H-minima transform is proposed to detect cell markers (seeds) within a connected component obtained from inner distance transform.

Object detection and segmentation can also be formulated into a graph cut problem [22], where pixels are modeled as the nodes. A graph cut segmentation algorithm minimizing an energy function was proposed in [23]. In [24], seed detections are implemented by dissecting the weighted graph using normalized cuts [25]. Some other graph based methods can be found in [18, 26, 27, 28, 29, 30, 31, 32].

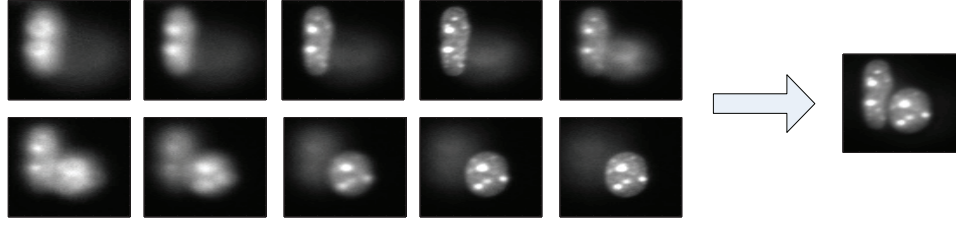


Figure 1.1: An all-in-focus image is synthesized from z-stack images.

A ridge detection based muscle fiber segmentation algorithm was proposed in [33]. Radial voting based methods [2, 34, 3] were proposed to locate the center of cells with a major assumption on round shaped cells, which does not hold in our case because myonuclei in muscle fibers contain both elongated ellipses and round circles. When voting based methods [33, 2, 34, 3] are applied to the cells with elliptical shapes, they tend to create false positive detections. Nuclei detection and segmentation methods based on Laplacian-of-Gaussian (LoG) with adaptive scale selection were reported in [1, 35]. Similarly, their method works better for touching cells with round shapes. Concave point detection based algorithm are proposed in [18, 36], however, it is often difficult to find a general rule for shape decomposition. Gradient vector diffusion [37] is proposed to detect blob-like objects in microscopic zebrafish images. The method is robust to noise, and can achieve accurate and consistent performance.

In this chapter, we have developed a novel algorithm for automatic myonuclear detection in isolated fixed skeletal muscle fibers stained with DAPI to visualize nuclei. The original z-stack images are presented in the left of Fig. 1.1. It can be observed that there exist the following challenges: 1) The myonuclei tend to exhibit a variety of circularity ratios, ranging from elongated ellipses to round circles. The round shape assumption therefore does not hold. 2) Some myonuclei have inhomogeneous staining intensities due to DAPI intercalating preferentially into heterochromatin, which creates some bright spots irregularly distributed in the myonuclei. This inhomogeneity tends to fail many current segmentation algorithms that require homogeneous intensity distribution of the object.

In this chapter, we have proposed an algorithm that can handle all these challenges. The contributions of this chapter are:

- A novel robust ellipse fitting based on heteroscedastic error-in-variables (HEIV) regression algorithm is applied to generate a sufficient number of ellipse fitting hypotheses based on the concave points and contour segments.
- A novel two stage sparse optimization model is proposed for robust sample and feature selection.
- A modified mean-shift clustering algorithm based on geometric inner-distance is used to merge the seeds and generate the final myonuclear detection results.

The rest of this chapter is organized as follows. The myonuclear detection algorithm is explained in detail in Section 2. The experimental results are described in Section 3. Finally, Section 4 concludes the chapter.

## 1.2 Method

Our algorithm consists of four steps: preprocessing, robust ellipse fitting, and refinement, and mean-shift clustering based on geodesic inner distance. The algorithm

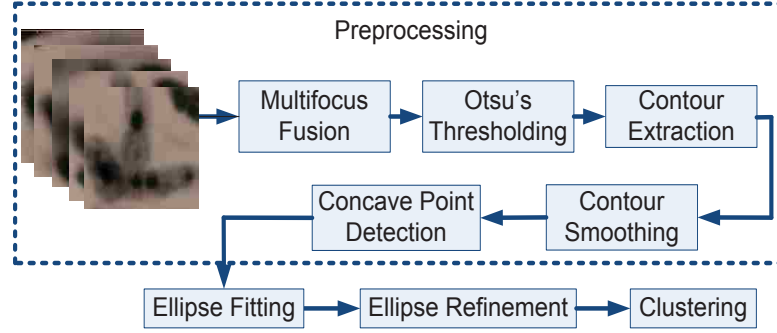


Figure 1.2: An overview of the proposed algorithm.

flowchart is shown in Figure 2.1. In the preprocessing step, a multifocus image fusion technique is applied to derive an all-in-focus image from the original z-stack images, as shown in Fig. 1.1. Because there exist touching myonuclei, a concave point detection method is used to detect the concave points after thresholding using Otsu's method [38], contour extraction and smoothing. A sufficient number of hypotheses of potential fitting ellipses are calculated with heteroscedastic error-in-variable (HEIV) regression. In the ellipse refinement stage, two stage sparse optimization is applied to find the representative training samples and discriminative cellular features. Based on these selected sparse samples and their corresponding representative features, a support vector machine (SVM) classifier is trained to identify the best ellipse that represents the myonuclei. Finally, a mean-shift clustering algorithm based on geodesic inner distance is used to merge multiple ellipse candidates to produce the final myonuclei detection results.

## Preprocessing

### Multifocus Image Fusion

In z-stack imaging, the microscope collects lights from both the in-focus plane and the out-of-focus planes. Therefore, each image consists of in-focus objects as well as out-of-focus objects. Motivated by [39], we have proposed a modified image fusion algorithm to compose a smooth multifocus image from the whole z-stack images. Let  $i = 1, 2, \dots, N$  denote the z-stack images, the magnitude of gradients of each image is calculated as

$$M_i(x, y) = \sqrt{I_{X(i)}^2(x, y) + I_{Y(i)}^2(x, y)}, \quad (1.1)$$

where  $I_{X(i)}^2(x, y)$  and  $I_{Y(i)}^2(x, y)$  are the horizontal and vertical gradients of the image  $i$ , respectively. Different from [39] which picks the pixel  $I_i(x, y) = \operatorname{argmax}_i M_i(x, y)$  as the synthesized image intensity  $I_s(x, y)$ , a linear combination of all the pixel values in the z-stack is used to calculate  $I_i(x, y)$

$$g_i(x, y) = \frac{M_i(x, y)^k}{\sum_{i=1}^N M_i(x, y)^k}, \quad k = 3, \quad (1.2)$$

$$I_s(x, y) = \sum_{i=1}^N g_i(x, y) I_i(x, y). \quad (1.3)$$

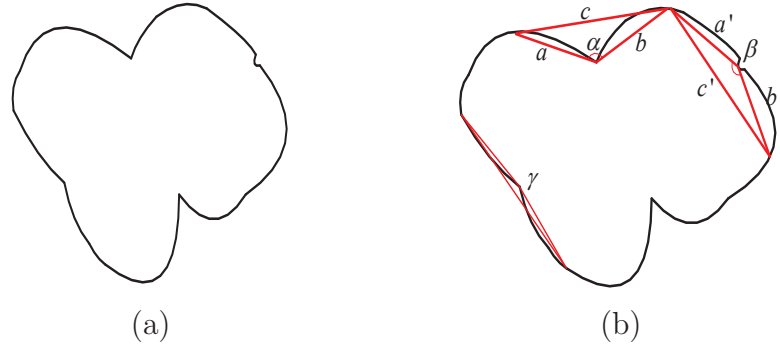


Figure 1.3: (a) Original contour. (b) Concave point detection and refinement.

Our image fusion algorithm can provide the final composed image with smooth boundaries, which greatly increase the robustness of the subsequent automatic detection procedure.

### Contour Smoothing and Concave Point Detection

Let  $I_{sc}(x, y)$  represent the binary image containing the contours of the objects in the synthesized image  $I_s(x, y)$ . Before applying the concave point detection algorithm to  $I_{sc}(x, y)$ , a contour smoothing algorithm [40] is applied to increase the robustness for concave point detection. The contour of each connected component is represented by Freeman chain code with eight directions, elliptical Fourier transform [41] is then applied to smooth the contour by keeping the first  $m$  ( $m = 20$  in our case) Fourier coefficients.

A concave point detection algorithm [18] is applied to each point of the contour. As shown in Fig. 1.3(b), some false concave points need to be removed. We first calculate an angle for each concave point using

$$\alpha = \arg \cos \frac{a^2 + b^2 - c^2}{2ab}. \quad (1.4)$$

As shown in (Fig. 1.3(b)), the concave point with  $\alpha < 165^\circ$  and the midpoint of  $c$  outside the contour is kept as candidate. The concave point with angle  $\gamma$  is removed because  $\gamma > 165^\circ$ . The concave point with angle  $\beta$  is removed because the midpoint of edge  $c'$  is inside the contour. The contour point with angle  $\alpha$  is kept as the true concave points.

### Ellipse Fitting and Refinement

#### Ellipse Fitting Using Heteroscedastic Errors-in-variables (HEIV) Regression

Heteroscedastic errors-in-variables (HEIV) regression is used to generate the **robust** fitting ellipses. Compared with some other traditional methods, HEIV has a weaker dependence on initialization and a faster convergence. Direct least-squares (DLS) method [42] is biased when the input data points are a short low-curvature segment of a whole ellipse as shown in Figure 1.4. Geometric distance minimized with Levenberg-Marquardt (LM) [43] is sensitive to the initialization, and the initial value could be biased if it is obtained by DLS method [44]. We also include fitting result

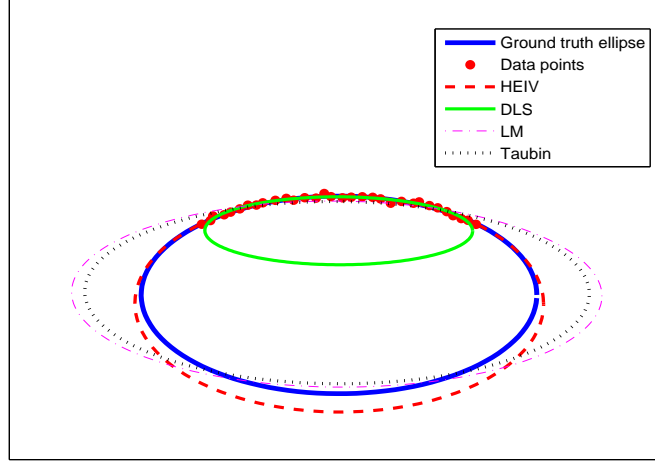


Figure 1.4: A demonstration of various ellipse fitting results.

of Taubin's method [45] in Figure 1.4 for comparison purpose. In our algorithm, an ellipse is modeled by its linear form

$$\varphi(\mathbf{x}_{io}, \alpha, \boldsymbol{\theta}) = \alpha + \mathbf{z}(\mathbf{x}_{io})^T \boldsymbol{\theta} = 0, \quad (1.5)$$

where  $\alpha$  and the five dimensional vector  $\boldsymbol{\theta}$  are the ellipse parameters,  $\mathbf{x}_{io}$  is the noise-free data, and

$$\mathbf{z}(\mathbf{x}_{io}) = [x_{1io} \ x_{2io} \ x_{1io}x_{2io} \ x_{1io}^2 \ x_{2io}^2], \quad (1.6)$$

where  $\mathbf{z}(\mathbf{x}_{io})$  is used to represent the five dimensional carrier dependent on the data. The true data is corrupted by additive noise

$$\mathbf{x}_i = \mathbf{x}_{io} + \delta_i, \quad \delta_i \sim GI(\mathbf{0}, \sigma^2 \mathbf{C}_{x_i}), \quad (1.7)$$

where  $GI(\boldsymbol{\mu}, \mathbf{C})$  represents Gaussian distribution with mean  $\boldsymbol{\mu}$  and covariance  $\mathbf{C}$ . Because the noise corrupting the true data  $\mathbf{x}_{io}$  appears in the carrier vector, the carriers are not independent from each other. HEIV fitting algorithm employs the *errors-in-variables* (EIV) model, and apply the HEIV algorithm to iteratively compute the maximum likelihood estimators in the linear model by solving

$$[\hat{\alpha}, \hat{\boldsymbol{\theta}}, \hat{\mathbf{x}}_i] = \arg \min_{\alpha, \boldsymbol{\theta}, \mathbf{x}_{io}} \sum_{i=1}^n (\mathbf{x}_i - \mathbf{x}_{io})^T C_{x_i}^{-1} (\mathbf{x}_i - \mathbf{x}_{io}), \quad (1.8)$$

subject to constraint (1.5) and

$$4\theta_4\theta_5 - \theta_3^2 = 1. \quad (1.9)$$

The HEIV algorithm exploits the dependency between  $\alpha$  and  $\boldsymbol{\theta}$ , and iteratively computes the solution by solving a generalized eigenvalue problem

$$\mathbf{S}(\hat{\boldsymbol{\theta}})\hat{\boldsymbol{\theta}} = \lambda \mathbf{C}(\hat{\boldsymbol{\theta}})\hat{\boldsymbol{\theta}}, \quad (1.10)$$

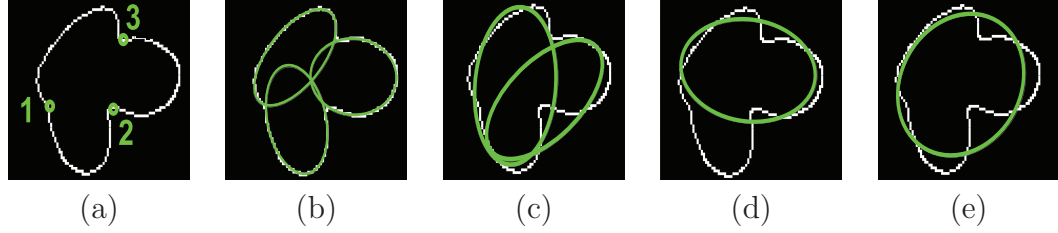


Figure 1.5: Robust ellipse fitting using HEIV regression.

where  $\mathbf{S}(\hat{\boldsymbol{\theta}})$  and  $\mathbf{C}(\hat{\boldsymbol{\theta}})$  are weighted scatter matrix and weighted covariance matrix, respectively. In each iteration a new estimate  $\hat{\boldsymbol{\theta}}$  is calculated by finding the eigenvector corresponding to the smallest eigenvalue, and a new  $\hat{\alpha}$  is computed from  $\hat{\boldsymbol{\theta}}$ . The new parameter estimators are used to update the new estimates of the true data  $\hat{x}_i$ , the noise variance  $\hat{\sigma}^2$ , and the moments of the carrier noise  $\boldsymbol{\mu}_{z_i}$  and  $\mathbf{C}_{z_i}$ . The iteration stops when the smallest eigenvalue approaches 1. This algorithm works well for both homoscedastic and heteroscedastic noises. The estimators obtained are unbiased. The proof of its unbiasedness can be found in [46].

In order to segment the touching myonuclei, robust ellipse fitting based on HEIV regression model is performed on the contour pixels. Assume there are  $c$  concave points for a contour, the original object contour is intersected by the concave points into  $c$  segments. We fit candidate ellipses using the different combinations of the contour segments. Thus, there are  $\binom{c}{k}$  segment combinations if we choose  $k$  segments to fit one ellipse. We empirically set  $k = \{1, 2, 3\}$  to make sure that a sufficient number of ellipses using HEIV regression are generated as input during the subsequent refinement procedure. One robust ellipse fitting example using HEIV regression model is shown in Fig. 1.5. Three concave points are marked with 1, 2, and 3 in Fig. 1.5(a). 7 candidate ellipses are fitted using the combinations of the 3 contour segments (Fig. 1.5(b)-(e)).

### Ellipse Feature Extraction

Given the ellipse fitting result calculated from Section 1.2, the next step is to generate representative image features. The following geometric features, summarized in Table I, are defined as:

**Set 1:** The most intuitive geometric feature to evaluate the accuracy of ellipse fitting is to measure whether or not the fitting ellipse matches with the boundaries of myonuclei. A set of morphological ratios are defined for this measurement. Given the fitting ellipse and the contour of the myonuclei, the overlapping ratios are calculated based on the overlapping areas of the fitting ellipse and the contour. Let  $r_{aoc} = \frac{A_o}{A_c}$  and  $r_{aoe} = \frac{A_o}{A_e}$ , where  $A_o$  denotes the overlapping area, and  $A_c$  and  $A_e$  denote the areas of the contour of myonuclei and fitting ellipse, respectively. In addition, the ratio  $r_{oace} = \frac{A_o}{A_c + A_e}$  is also calculated.

Considering robustness, the pixel-wise overlapping ratios are calculated. Let  $p_o$  denote the overlapping pixels between a fitting ellipse and the object, and  $p_c$  as the number of pixels of the contour. Then, we define contour pixel level overlapping ratio  $r_{oc} = \frac{p_o}{p_c}$ . Based on  $r_{oc}$ , we design an iterative procedure to assign a match-quality score to each fitting ellipse. In each iteration, we count the contour pixels overlapping with an ellipse, then sort the ellipses with respect to the number of their overlapping contour pixels. At the end of each iteration, the contour pixels that overlap with



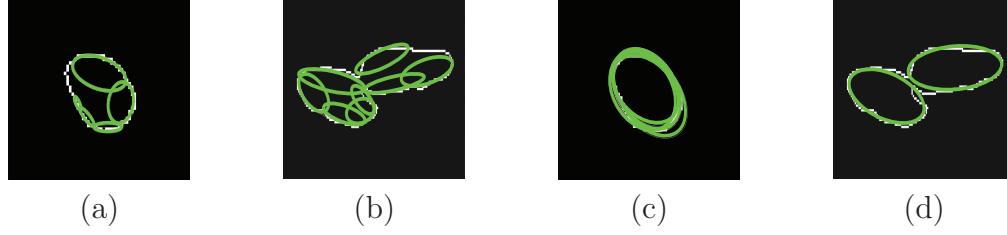


Figure 1.6: Examples to illustrate the **Set 3** features.

the highest ranked ellipse are removed, and  $r_{oc}$  is updated for each remaining ellipse. The iteration stops when there is a small fraction (decided by a threshold) of contour pixels left. Note that in each iteration, the ellipse that has the most overlapping pixels with object contour pixels will be assigned the highest rank. The match-quality of an ellipse is defined as the ranks of this fitting ellipse calculated during each iteration. To improve efficiency, we only record the ranks of an ellipse in the first three iterations. **Set 2:** The myonuclei are objects which have certainly biological meaningful areas. Therefore, the area of the ellipse  $A_e$ , the axis ratio  $r_{axis}$ , and the perimeter  $p_c$  and area  $A_c$  of the myonuclei contour are also considered as potential geometric features for classification.

**Set 3:** Concave point depth is a feature designed to distinguish the ellipses shown in Fig. 1.5(b) and (c)-(e). This is based on the observation that an accurate ellipse fitting should not have concave point deeply inside the ellipse. Considering this, for a given ellipse  $E_i$ , ( $i = 1, \dots, N$ ) and a set of concave points  $c_j$ , ( $j = 1, \dots, c$ ), concave point depth  $d_i$  is defined as the sum of squares of the Euclidean distances from the concave points to ellipse  $E_i$ :

$$d_i = \sum_j dist^2(c_j, E_i), \quad j \in \{j : c_j \text{ is in ellipse } E_i\}, \quad (1.11)$$

where  $dist(\cdot)$  denotes the Euclidean distance from  $c_j$  to  $E_i$ .

Because the center of an accurate fitting ellipse should not locate near the boundary, the distance between the center of the fitting ellipse and object boundary  $d_{ecc}$  is also calculated. This feature can help to remove suboptimal fitting ellipses whose centers are close to the object boundaries. As shown in Fig. 1.6(a)-(b) The fitting ellipses whose centers are close to the cell boundary, i.e.  $d_{ecc}$  is small, thus not valid candidates. Fig. 1.6(c)-(d) represent good ellipse fittings with larger  $d_{ecc}$ .

**Set 4:** The irregularity of the boundaries are defined as  $r_{irg} = \frac{n_c}{p_c}$ , where  $p_c$  denotes the perimeter of a myonuclei contour, and  $n_c$  represents the number of concave points detected. Two examples are shown in Fig. 1.7(a)-(b) and (c)-(d). Both cells shown are single cells. Fig. 1.7(b) is the ellipse fitting result of Fig. 1.7(a) that has high  $r_{irg}$ . Fig. 1.7(d) is the ellipse fitting result of Fig. 1.7(c) that has lower  $r_{irg}$ .

**Set 5:** A set of statistical features are calculated to capture the relationships among the ellipses generated from the same contour. Assume  $N$  ellipse fitting candidates are generated from the the segments of an object contour, and  $f_i$ ,  $i = (1, 2, \dots, N)$  represents one specific feature calculated for the  $i$ -th ellipse  $E_i$ :

$$f_{1i} = f_i - \frac{1}{N} \sum_{i=1}^N f_i, \quad (1.12)$$

$$f_{2i} = f_i - \mathbf{median}(f_1, f_2, \dots, f_N), \quad (1.13)$$

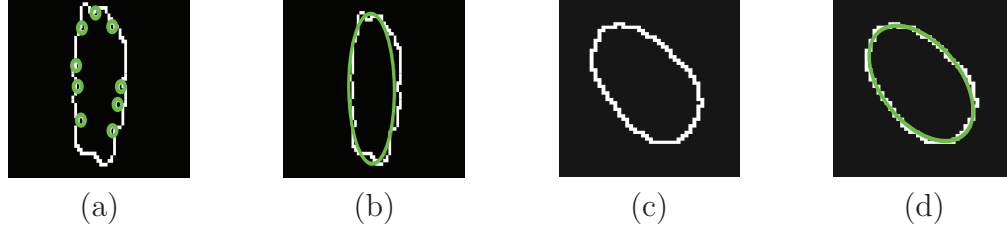


Figure 1.7: Examples to illustrate the **Set 4** features.

$$f_{3i} = f_i - \mathbf{max}(f_1, f_2, \dots, f_N), \quad (1.14)$$

$$f_{4i} = f_i - \mathbf{min}(f_1, f_2, \dots, f_N), \quad (1.15)$$

where the functions **median**( $\cdot$ ), **max**( $\cdot$ ) and **min**( $\cdot$ ) computes the median, maximum and minimum value of the input feature vector. These statistical features capture the inter-group variance of one ellipse fitting compared with the whole group of fitting ellipses for the same object contour. These statistical features are calculated for each feature in **Set 1** and **Set 3**.

**Set 6:** The following two features are also considered in the classification algorithm: 1) Distance from fitting ellipse centroid to the object centroid. 2) Average distance from one ellipse centroid to the centroids of all the other fitting ellipses for the same object contour.

### Learning Based Ellipse Refinement Using Two-stage Sparse Optimization

In the object space, not all the training samples are representative ellipse-myonuclei cases that need to or should be used for learning. Similarly, in the feature space, a discriminative feature set can significantly improve the classification performance considering the curse of dimensionality. We have proposed a novel two-stage sparse optimization to 1) select the most representative training samples in the object space, and 2) identify the most discriminative features in the feature space.

#### Training Example Selection Using Dictionary Learning by K-Selection:

In this step, we assume that all the training samples can be sparsely represented by a subset of representative samples (dictionary bases). Only these typical samples are needed to train the ellipse refinement classifier. Our recently proposed K-selection [47] algorithm is used to select a set of most representative training samples from the original training dataset. For the given training sample set  $E = \{\mathbf{e}_i | i = 1, 2, \dots, N\}$ , where  $\mathbf{e}_i$  denotes the feature vector of the  $i$ -th training sample, we assume a dictionary  $B = \{\mathbf{b}_i | i = 1, 2, \dots, K\}$  exists such that all the training samples can be represented by a linear combination of the selected bases in  $B$ . The basis samples in  $B$  can be found by performing dictionary update and sparse coding alternatively:

$$\begin{aligned} \min_{\mathbf{b}_k \in B, \mathbf{x}_i} \sum_{i=1}^N \|\mathbf{e}_i - \sum_{k=1}^K \mathbf{b}_k x_{ik}\|^2 + \lambda \|\mathbf{d}_i \odot \mathbf{x}_i\|^2, \\ s.t. \quad \mathbf{1}^T \mathbf{x}_i = 1, \quad \forall i, \end{aligned} \quad (1.16)$$

where  $\mathbf{b}_k$  is  $k$ -th feature vector selected as the basis vector from the original training sample set,  $\mathbf{x}_i$  is the representation coefficients, and  $\mathbf{d}_i$  is the distance between  $\mathbf{e}_i$  and the basis vectors.

The dictionary is updated using a projection-based gradient descent method. Within each iteration, we choose sample  $e_l$  to replace basis  $b_t$

$$\mathbf{e}_l^* = \arg \max_{e_l} \frac{-\nabla f_t(\mathbf{e}_l - \mathbf{b}_t)^T}{\|-\nabla f_t\|_2 \|\mathbf{e}_l - \mathbf{b}_t\|_2}, \quad (1.17)$$

where  $\nabla f_t$  is the gradient of cost function (1.16) with respect to basis  $\mathbf{b}_t$ . We accept  $\mathbf{e}_l^*$  if the replacement reduces the value of the cost function, that is the selected basis has the largest correlation between the displacement and the negative gradient direction. The last term in (1.16) models the locality constraint, which encourages each sample to be represented by its local bases and allows the optimization problem to be efficiently solved in a much smaller local system. Locality-constraint linear coding [48] is applied to (1.16) for sparse coding. In our algorithm, we perform this  $K$ -selection to the positive and negative samples separately.  $K$ -selection does not assume that the data is low-rank. For each sample, it does not require all the samples to be used during the optimization procedure, either. These characteristics are different from the recent selection-based dictionary learning methods [49, 50].

**Feature Selection Using Sparse Representation:** As shown in Table 1.1, in total we have extracted  $P = 43$  morphological features for learning based fitting ellipse refinement. In order to improve the classification performance, a sparse representation model is employed to select the most discriminative features:

$$\begin{aligned} \min_{\alpha, \beta} \sum_{i=1}^N \omega_i \log(1 + e^{-z_i(\alpha^T f_i + \beta)}), \\ \text{s.t. } \|\alpha\|_1 \leq \rho, \alpha \geq \mathbf{0}, \end{aligned} \quad (1.18)$$

where  $N$  is the number of training ellipses,  $\omega_i$  and  $f_i \in \mathbb{R}^{P \times 1}$  represent the weight and the feature for the  $i$ -th ellipse, respectively. The binary scalar  $z_i$  denotes the ellipse label:  $z_i = +1$  for positive and  $z_i = -1$  for negative,  $\beta$  is a scalar representing the intercept, and  $\rho$  is the parameter controlling the sparsity of  $\alpha$ . Due to the  $l_1$  norm constraint, the solution  $\alpha^* \in \mathbb{R}^{P \times 1}$  to (1.18) is sparse with nonzero elements corresponding to the selected discriminative features. Based on  $\alpha^*$  with  $L$  nonzero elements, all the features are projected onto a lower-dimensional, discriminative feature space, which can benefit the subsequent classification. The equation (1.18) is optimized with the widely used Sparse Learning Package (SLEP) [51].

Equation (1.18) is a supervised method which aims to select discriminative features with respect to the subsequent classification as well as removing redundant information. In comparison with those unsupervised feature selection methods such as PCA [52], ISOMAP [53], and LLE [54], our feature selection method is designed to optimize the classification performance. Boosting [55] based feature selection may have performance similar to sparse representation due to their common logistic regression nature. However, boosting is relatively less efficient compared with sparse representation for feature selection [56]. SVM-RFE feature selection does not guarantee the selected features are most relevant with minimal redundancy [57]. Other methods, like Laplacian score [58], trace ratio [59], relief and reliefF [60], and SPEC [61], and HSIC [62], evaluate features individually and thus are not specifically designed to handle redundant features.

## Classification and Inner Geodesic Distance Based Clustering

After two stage sparse optimization, the selected training samples are used to train a SVM classifier. The classifier outputs are shown in Fig. 1.8(a). Note that the

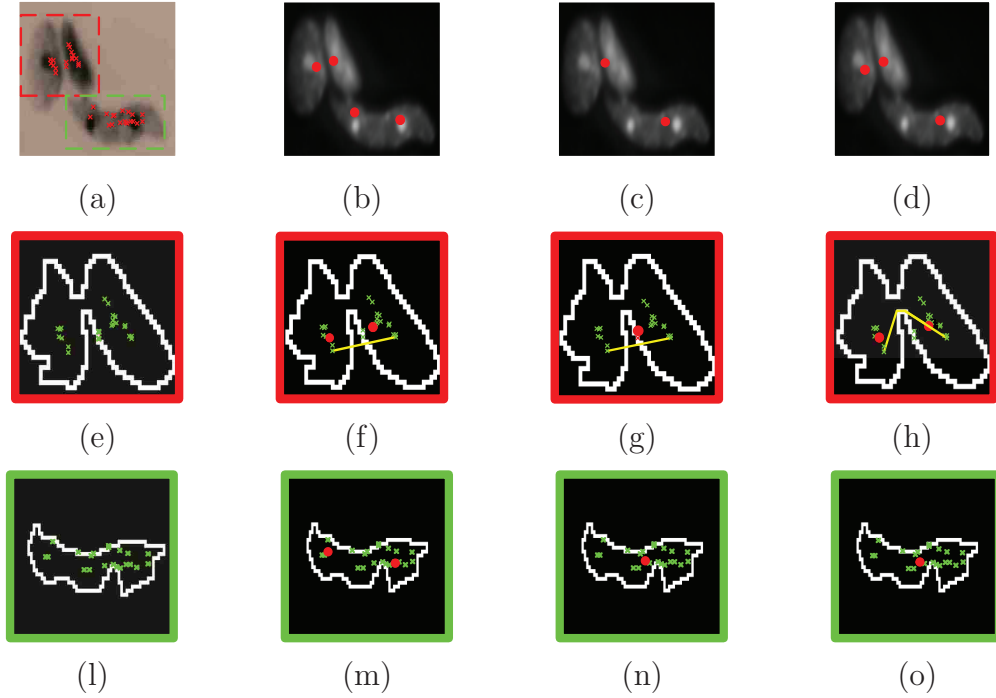


Figure 1.8: Mean-shift clustering based on inner distance.

smaller markers are the centers of the ellipses selected by the classifier. The ground-truth myonuclei detection should identify two touching nuclei on the top and one single nuclei in the bottom (in total three myonuclei). This is a challenging problem because of the bright dots irregularly distributed inside the myonuclei. This is due to the DAPI intercalating preferentially into heterochromatin. The yellow lines in 1.8(f) and 1.8(g) denote a sample Euclidean distance between two seeds. The yellow line in 1.8(h) denotes a sample inner distance between two seeds. 1.8(b) shows the clustering results based on Euclidean distance with bandwidth  $bwd_c = 10$ . 1.8(c) shows the clustering based on Euclidean distance with bandwidth  $bwd_c = 14$ . As can be seen that it is difficult to find a unified bandwidth that produces accurate detection results for both cases. However, using inner distance, a unified bandwidth ( $bwd_c = 14$ ) can be used and the accurate detection results for both cases are shown in 1.8(d).

In order to achieve the correct final detection, we have designed an inner distance based mean-shift clustering algorithm to merge all the candidates. Our method consists of 1) inner-distance calculation to compute the inner-distance matrix, and 2) mean-shift based clustering to locate the final seeds.

The inner-distance is calculated as the length of the shortest connecting pathes that only lay inside the object. For example, in Fig. 1.8(g), the direct line connecting the two center points represents Euclidean distance because the pathes are not entirely inside the object. On the contrary, the inner geodesic distance is calculated by first building a graph with the ellipse centers and the concave points as vertices and the links connecting these vertices inside the contour as edges, then running a shortest distance algorithm in the graph. An example of inner-distance graph is shown in Fig. 1.8(h). Since the inputs of the mean shift clustering are coordinates of the points, the inner-distance matrix will be converted into a new coordinate system by harboring the origin at one of the two points and calculating the other relevant distances.

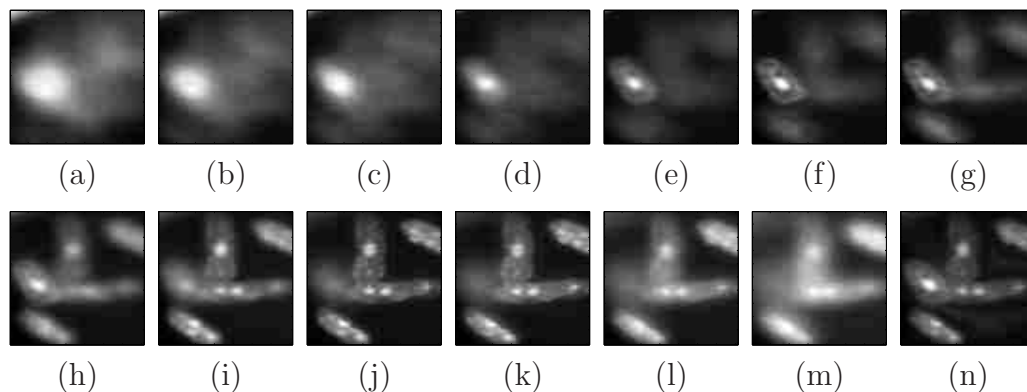


Figure 1.9: An all-in-focus image (n) synthesized by multi-image fusion.

The reason that we do not choose standard Euclidean distance is demonstrated in Fig. 1.8. Inner distance is intuitively correct because the real distance between two seeds should be the paths within the object, instead of a direct line that might cross the cell boundaries [18]. As shown in Fig. 1.8(a), Euclidean distance based clustering will face some serious challenges in selecting proper clustering bandwidth (Fig. 1.8(b) or (c)). On the other hand, based on inner geodesic distance, correct clustering results have been obtained using one unified bandwidth, as we shown in Fig. 1.8(d). Inner-distance is proven to be quite effective in natural shape classification [63]. Some clustering results are shown in Fig. 1.8. Note that all the clustering results based on inner geodesic distance are obtained with the same clustering bandwidth  $bwd_c = 14$ .

### 1.3 Experimental Results

All animal procedures were conducted in accordance with institutional guidelines for the care and use of laboratory animals as approved by the Animal Care and Use Committee at the University of Kentucky. Adult (4 months of age) male C57Bl6 mice were injected intraperitoneally with ketamine (100mg/kg) and xylazine (10mg/kg) and euthanized by cervical dislocation. Plantaris muscles were fixed in situ at resting length by fixation in 4% paraformaldehyde for 48 hours. Single muscle fibers were subjected to 40% NaOH digestion and manually isolated as previously described [64]. Single fibers were stained with DAPI and nuclei from 15-25 fibers per animal counted. Fibers were imaged by z-stack analysis using the AxioImager M1 microscope.

In total we have collected over 500 multifocus z-stack images (over 1500 myonuclei) from 42 individual isolated single muscle fiber. A set of image patches cropped from some randomly selected z-stack images and their corresponding all-in-focus fused image are shown in Fig. 1.9. A support vector machine classifier is trained using ellipses generated from 7 fused images (1000 positive samples and 3000 negative samples), and the rest 35 cases are used for testing. The ground-truth ellipses and seeds are manually marked for each cell. In order to evaluate and validate the proposed algorithm, we have presented the experimental results on validating 1) the effectiveness of the geometric features described in Section 1.2 on ellipse refinement, 2) sparse representation based sample and feature selection methods described in Section 1.2, 3) the effectiveness of the inner-distance based clustering (1.2), and 4) the overall comparative myonuclei detection results.

We implemented our algorithm using MATLAB with the SVM package [65] on a PC machine with i3 CPU and 16Gb memory. The SVM classifier uses Gaussian

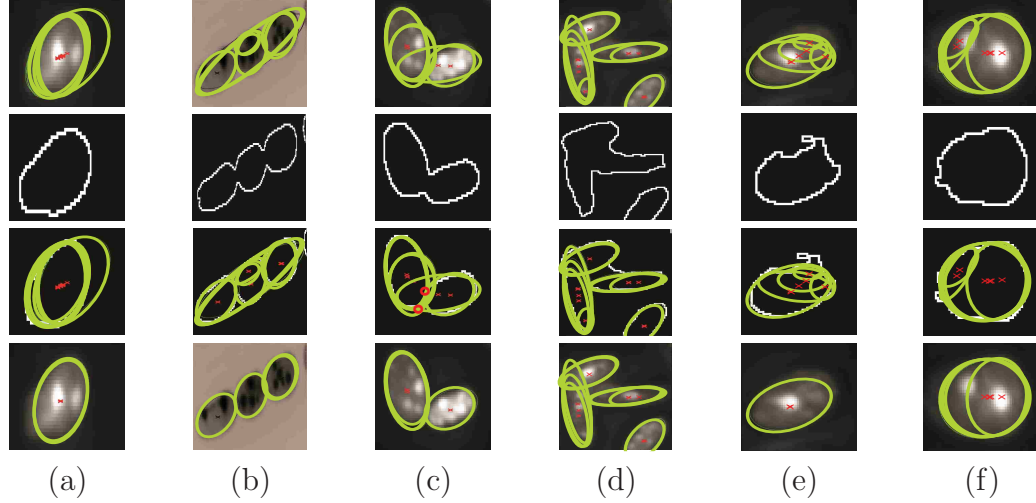


Figure 1.10: Examples showing effects of the geometric features.

kernel with precision  $\gamma = 0.3$  and penalty 1 by cross validation. The bandwidth for mean-shift clustering is empirically set to 16 pixels. For the data with elongated or larger cells, a large window bandwidth is preferred. The selection of  $K$  in (1.16) interacts with the size of training samples. In practice a large  $K$  is chosen when the data have significant variations, and 15% of the training sample size is found to be sufficient to approximate the data. Usually the algorithm takes less than 1 minute to count one all-in-focus image.

The  $k$  in Equation (1.2) determines the sharpness of the fused image. A smaller  $k$  will generate a fused image with higher contrast and vice versa. In our experiment,  $k = 3$  produces enough contrast. In order to avoid the local false concave points, the contours are smoothed by elliptical Fourier descriptor, and its first  $m$  coefficients are kept.  $m = 20$  is chosen in our experiments.

### Geometric Features

In this section we illustrate the effectiveness of the geometric features for ellipse refinement in Fig. 1.10. The first row of Fig. 1.10 shows the original ellipse fitting results obtained from Section 1.2. The second row shows the contours. The third row represents the contours and the fitted ellipses. The fourth row lists the ellipses selected by the learning based ellipse fitting refinement classifier.

**Set 1** evaluates the extent of matching between object boundaries and fitting ellipses. In Fig. 1.10(a), it is clear that the classifier can successfully reject some false fitting ellipses that have lower overlapping ratios.

The features  $A_e$  and  $A_c$  in **Set 2** help to differentiate the valid fitting ellipse from false fittings by measuring their areas. As we show in Fig. 1.10(b), although the largest (longest) ellipse exhibits better overlapping ratios, it also encloses a larger area. In addition, the axis ratio  $r_{axis}$  and contour perimeter  $p_c$  also indicate that the largest ellipse is suboptimal. Considering these regularizations, the ellipse refinement classifier has rejected this candidate, as shown in Fig. 1.10(b).

In **Set 3**, the concave point depth is designed for the touching myonuclei. We put one typical case of the touching myonuclei in Fig. 1.10(c). The red circles in the third row are concave points. It can be observed that this feature enables the classifier to reject the two ellipses containing concave points. The effect of feature  $d_{ecc}$  is shown

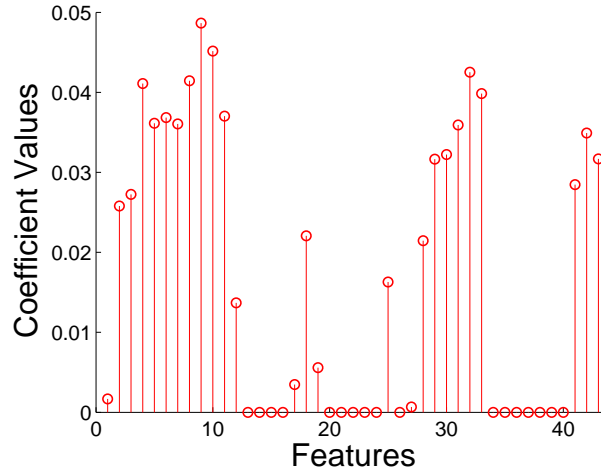


Figure 1.11: The selected discriminative features by sparse representation.

in Fig. 1.10(d). The ellipses whose centers are close to the contour boundary are removed.

The contribution of the irregularity measurement is shown in Fig. 1.10(e). This feature is designed to enable a more robust classifier in the presence of extremely irregular contours. Compared with the myonuclei with smooth contours, these irregular ones can generate higher values with respect to irregularity measurements of the fitting ellipses. This enables the classifier to differentiate the ellipses having lower overlapping ratios with higher irregularity measurements, which may still be valid ellipse fitting results.

The **Set 5** features is designed to capture the statistical properties of fitting ellipses within one contour. The effect of the two distances features in **Set 6** is shown in Fig. 1.10(f). These features force the classifier to select the ellipses whose centroids locate near to the centroid of the contour and away from the contour boundary.

The parameter  $\rho = 180$  is used in the sparse representation-based feature selection model in (1.18), and a set of most discriminative features is presented in Fig. 1.11. Those features with zero coefficient values are non-discriminative ones, which contain the  $f_{2i}$  (except the median feature for  $match_{qual2}$ ) and  $f_{3i}$  in Table 1.1. The mean features  $f_{1i}$  for the  $r_{aoc}$ ,  $r_{aoe}$ , and  $r_{oace}$  in Table 1.1 are not considered as important features either. On the other hand, the ranking scores  $match_{qual1}$ ,  $match_{qual2}$ ,  $match_{qual3}$ , and their corresponding min features  $f_{4i}$  are considered as the most significant features, since they iteratively evaluate the accuracy of an fitted ellipse based on the pixel-wise contour/fitting ellipse overlapping ratio. The selected features based on sparse representation is denoted with bold font in Table 1.1: Feature Index.

## Sample and Feature Selection

### Sparse Representation for Training Sample Selection

In our algorithm, the purpose for training sample selection is to learn a compact dictionary whose element is directly selected from the original training dataset. This approach is different from the widely used bag-of-words (BoW) model [66, 67] and spatial pyramid matching (SPM) [68] method for object recognition. In BoW model, the elements (visual words) in the codebook are not selection based, and are often learned through some clustering methods such as K-means without considering

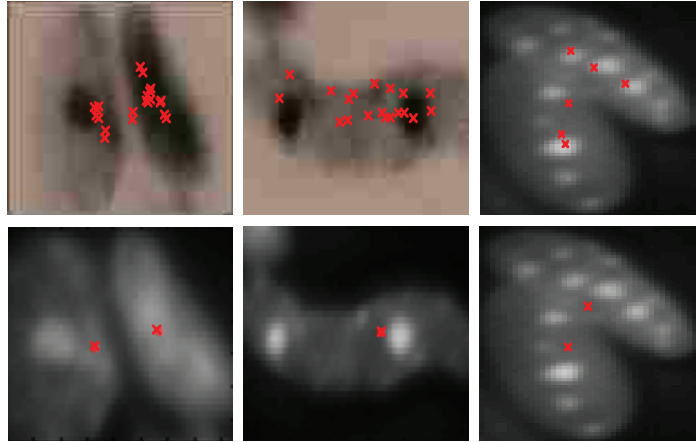


Figure 1.12: The mean-shift clustering based on inner distance.

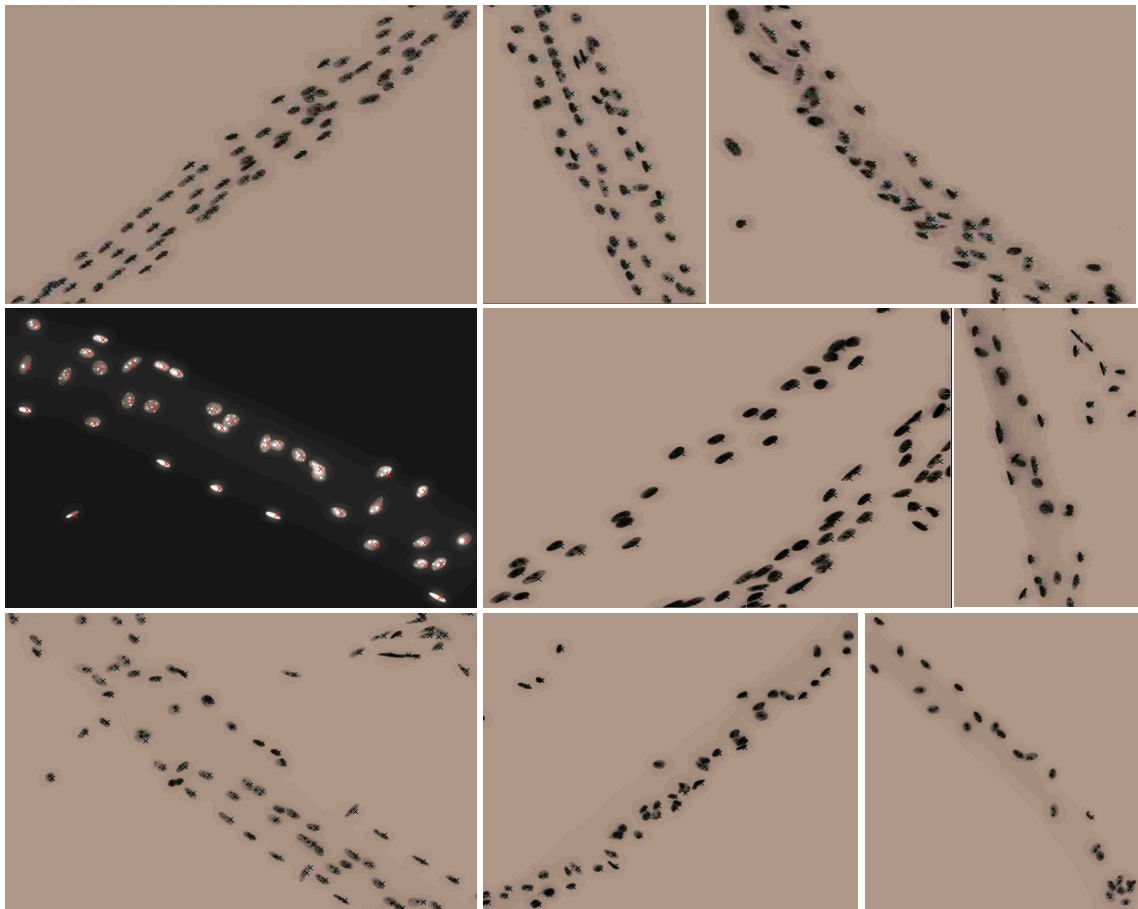


Figure 1.13: Detection results of nine randomly selected image patches.

sparseness. In order to compare these two different dictionary learning approaches, these two methods were evaluated based on the classification accuracy in finding correct ellipse fitting candidates for myonuclei detection.

In the comparative experiment, 4000 ellipse fitting candidates are randomly di-



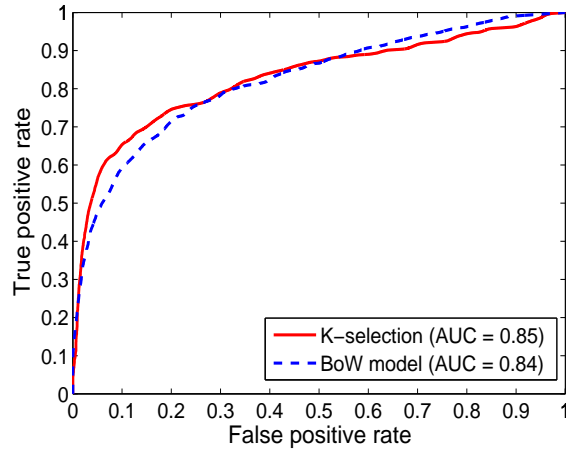


Figure 1.14: The ROC curves using dictionary learning by K-selection v.s. BoW model.

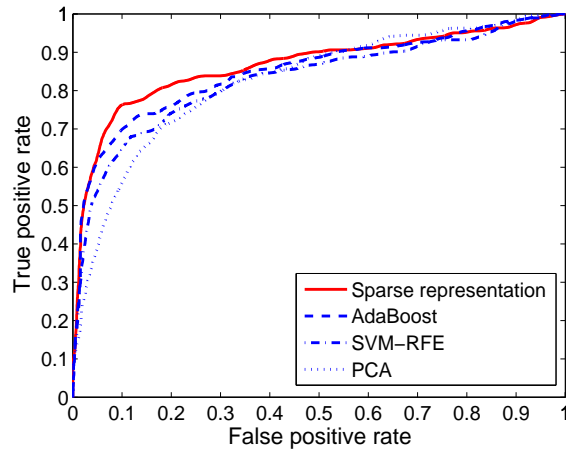


Figure 1.15: Classification performance of four feature selection methods.

vided into training (1600, 400 positive and 1200 negative) and testing (2400, 600 positive and 1800 negative) datasets, respectively. 15% of the training samples were selected by K-selection and the same amount of visual words were calculated in BoW model for fair comparison. The same classifier (linear kernel SVM) using the same parameters are trained for evaluation. In order to avoid bias introduced in the feature selection step, all features are used to evaluate the two different dictionary learning methods. The ROC curve is shown in Figure 1.14, and the areas under the ROC curves (AUCs) are also presented in the legend. As one can tell, sparse representation based sample selection provides better results than BoW for our application with an average  $AUC = 0.85$  compared with  $AUC = 0.84$  using BoW model.

### Sparse Representation for Feature Selection

In order to justify the proposed sparse representation based feature selection method, our approach was compared with three state-of-the-arts, including PCA, AdaBoost [55], and SVM-RFE [57]. PCA achieves linear dimension reduction by removing the principal components corresponding to smaller eigenvalues. In this way the original data vector can be represented in a lower dimension space. In AdaBoost, each weak

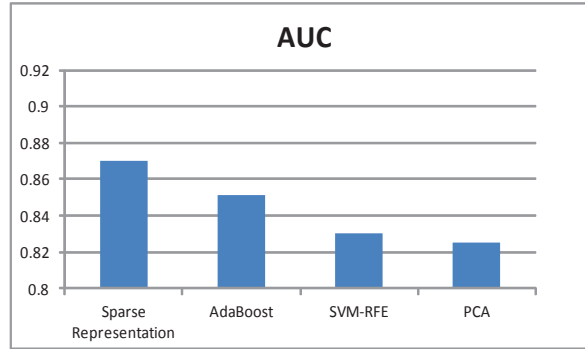


Figure 1.16: Comparison of the average AUCs using four feature selection methods.

classifier corresponds to one single image feature, and the final strong classifier not only represent the ensemble of all weak learners, but can also be used for feature selection by observing each weak learner’s weight. SVM-RFE is an iterative method [69, 70]. In each iteration it trains a linear SVM classifier and ranks the features with respect to their weights. The feature with the lowest weight is removed. The final output is a ranking of all the features in terms of their importance.

For fair comparison, the same set of features listed in Table 1.1 is used in these algorithm. Similar to Section 1.3, the performance is measured based on the classification accuracy using the 2400 testing samples. The ROC curves are shown in Figure 1.15. It can be observed that the proposed feature selection method outperforms the other three methods. The performance of AdaBoost is close to sparse feature selection method. SVM-RFE can provide satisfactory results but is still outperformed by the proposed method. PCA is an unsupervised method, and thus it is not optimized to provide best classification results. The AUCs of four methods are listed in Figure 1.16. In addition, the statistics (sensitivity, specificity, and accuracy) of the true positive rate (TPR) with the false positive rate being fixed at 0.2 are also presented in Table 1.2. All these detailed quantitative experiments confirm that sparse feature selection algorithm provides the best results classifying ellipse fitting candidates for robust myonuclei detection.

### Inner-distance Based Clustering

The performance of inner-distance based clustering is shown in Fig. 1.12. The first row denotes the classifier’s initial output. Each red dot denotes the center of one fitting ellipse. The second row demonstrates the inner-distance based clustering results. The ground truth annotation for the myonuclei detection should be two touching myonuclei for column 1, one myonuclei for column 2, and two touching myonuclei for column 3. It is obvious that in the second row, the inner distance based clustering can produce accurate results for all three cases. Through the whole experiments, we set the clustering bandwidth to  $bwd_c = 16$ . Some myonuclei detection results of nine fused image after inner-distance based clustering is shown in Fig. 1.13.

### Comparative Experiments

The proposed algorithm is compared with three recent state-of-the-art cell detection methods: Laplacian-of-Gaussian filters (LoG) [1], iterative radial voting (IRV) [2], and single-pass voting (SPV) [3]. Several representative image patches using different algorithm are shown in Fig. 1.17. For all the comparison experiments, we tried many possible parameters and configurations to generate the best results for the other methods used for comparison. As one can tell, it is difficult for LoG to handle

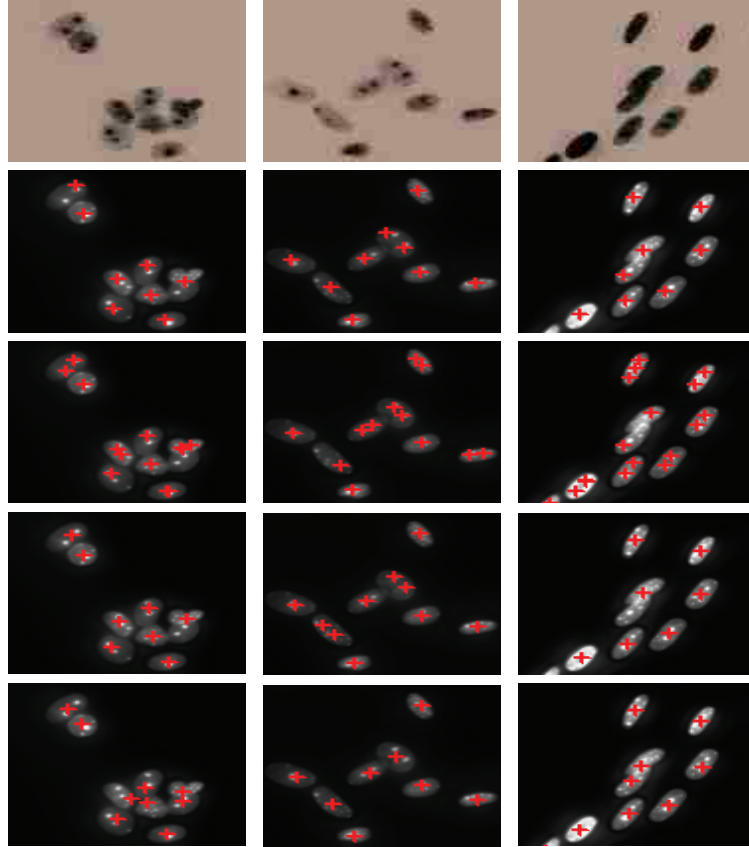


Figure 1.17: Performance comparison with LoG [1], IRV [2], and SPV [3].

touching cells and inhomogeneous intensity, while IRV and SPV may fail on cells with elongated ellipse shape, because they all assume round shape cells. Meanwhile, it is often difficult for IRV and SPV to create a general rule for parameter settings on an image containing cells with different sizes and shapes. However, the proposed algorithm is more robust with respect to touching cells exhibiting a large variations of scales, shapes, and especially inhomogeneous intensity distributions. This can be attributed to the robust ellipse fitting using HEIV regression, two stage sparse optimization model, and inner distance based mean-shift clustering in this proposed algorithm.

For quantitative comparison, we have measured the Euclidean distances between the manually annotated seeds and those created by the proposed automatic algorithm. Pixel-wise detection accuracy is listed in Table 1.3. It is obvious that the proposed method produces best accuracy with respect to both mean errors and standard deviations, representing high detection accuracy and robustness.

Table 1.4 shows the seed detection evaluation metrics including missing rate ( $MR$ ), over-detection rate ( $OR$ ), effective rate ( $ER$ ), precision, recall, and  $F_1$  score. The  $MR$  or  $OR$  means no seeds or more than one seed are detected for one ground-truth cell, respectively. The  $ER$  is calculated by evaluating the ratio between the number of detected seeds and the ground truth seeds, which measures the robustness to background clutter with  $ER = 1$  indicating the strongest robustness. Precision ( $P$ ), recall ( $R$ ) and  $F_1$  score are defined as  $P = \frac{TP}{TP+FP}$ ,  $R = \frac{TP}{TP+FN}$ , and  $F_1 = \frac{2*P*R}{P+R}$ . True positive ( $TP$ ) is defined as a detected seed that is inside a circular region with

a radius  $r = 8$  pixels centered at the ground truth seed. If it is outside this circular region, the detection is treated as false positives (FP). False negatives (FN) are defined as the missing detections.

As we show in Table 1.4, LoG is sensitive to image background noise, SPV may have higher FN, and IRV gives relatively low  $P$  and  $R$  values. On the contrary, the proposed method produces the highest  $P$  value without sacrificing the accuracy of  $R$ . For fair comparisons, the  $MR$  and  $OR$  are excluded when we evaluate the pixel-wise accuracy in Table 1.3.

Table 1.1: A summary of the geometric features for learning based ellipse refinement.

Sets	Symbols	Feature Index in Figure 1.11	Definitions
1	$r_{aoc}$	<b>4</b>	The ratio of the overlapping area with respect to the contour area.
	$r_{aoe}$	<b>5</b>	The ratio of the overlapping area with respect to the ellipse area.
	$r_{oace}$	<b>6</b>	The ratio of the overlapping area with respect to the sum of the ellipse area and the contour area.
	$match_{qual1}$	<b>8</b>	The match-quality rank in iteration 1.
	$match_{qual2}$	<b>9</b>	The match-quality rank in iteration 2.
	$match_{qual3}$	<b>10</b>	The match-quality rank in iteration 3.
2	$A_e$	<b>2</b>	The area of an ellipse.
	$r_{axis}$	<b>3</b>	The ratio of the major and minor axis of an ellipse.
	$A_c$	<b>11</b>	The area of a myonuclei contour.
	$p_c$	<b>7</b>	The perimeter of a myonuclei contour.
3	$d_i$	<b>1</b>	The concave point depth of the $i$ -th ellipse generated for one contour.
	$d_{ecc}$	<b>42</b>	The distance from the center of an ellipse to its contour.
4	$r_{irg}$	<b>12</b>	The measure of the irregularity (smoothness) of the contour.
5	$f_{1i}$	13-16, <b>17-19</b>	The group of features based on the features in Set 1-2 and feature $d_i$ in Set 3. For a specific feature $f_i$ , ( $i = 1, 4, 5, 6, 8, 9, 10$ ) and a group of ellipses generated from a contour, calculate $f_{1i}$ for each ellipse by subtracting the mean of $f_i$ of all the ellipses in this group from $f_i$ .
	$f_{2i}$	20-24, <b>25, 26</b>	Similar to $f_{1i}$ , for an ellipse and the group of ellipse generated from the same contour, subtract the median of $f_i$ , ( $i = 1, 4, 5, 6, 8, 9, 10$ ) of all the ellipses in this group from $f_i$ of this ellipse.
	$f_{3i}$	34-40	Similar to $f_{1i}$ , subtract the maximum value of the $f_i$ , ( $i = 1, 4, 5, 6, 8, 9, 10$ ) of all the ellipses in the same group.
	$f_{4i}$	<b>27-33</b>	Similar to $f_{1i}$ , subtract the minimum value of the $f_i$ , ( $i = 1, 4, 5, 6, 8, 9, 10$ ) of all the ellipses in the same group.
6	$d_{cc}$	<b>41</b>	The distance from ellipse centroid to its contour centroid.
	$d_{aee}$	<b>43</b>	The average distance from one ellipse centroid to the centroids of the other ellipses of the same contour.

Table 1.2: The comparison of four feature Selection methods

Methods	TPR	Sensitivity	Specificity	Accuracy
AdaBoost	0.76	<b>0.81</b>	0.82	0.82
SVM-RFE	0.74	0.80	0.82	0.82
PCA	0.72	0.79	0.80	0.80
Proposed	<b>0.81</b>	<b>0.81</b>	<b>0.83</b>	<b>0.83</b>

Table 1.3: The pixel-wise seed detection accuracy compared with ground truth

	<i>Mean</i>	<i>Standard Deviation</i>	<i>Min</i>	<i>max</i>
LoG [1]	3.72	4.22	0.55	7.99
IRV [2]	4.28	3.86	0.24	<b>7.93</b>
SPV [3]	2.99	3.54	<b>0</b>	7.96
Proposed	<b>2.6</b>	<b>2.90</b>	0.17	<b>7.93</b>

Table 1.4: The comparative performance measured by precision and recall

	<i>MR</i>	<i>OR</i>	<i>ER</i>	<i>P</i>	<i>R</i>	<i>F<sub>1</sub></i>
LoG [1]	0.27	0.003	1.73	0.86	0.94	0.90
IRV [2]	0.31	0.34	1.69	0.83	0.90	0.86
SPV [3]	0.21	<b>0</b>	<b>0.97</b>	0.89	0.94	0.91
Proposed	<b>0.12</b>	<b>0</b>	1.02	<b>0.93</b>	<b>0.96</b>	<b>0.94</b>

## Chapter 2 Nuclei Detection in Histopathological Brain Tumor Images

### 2.1 Introduction

A rising of brain tumor incidences has been reported in [71]. Successful prognostic stratification, treatment outcome prediction, and therapy planning depends on consistent, reproducible, and accurate analysis of digitized histopathological specimens [72, 73]. Current manual analysis of histopathological slides is not only laborious, but also subject to inter-observer variability. Computer-aided diagnosis (CAD) systems have attracted increasing interests [74]. In CAD systems, cell detection is usually a prerequisite step [75, 76].

Cell detection for histopathological images has been studied widely. A brief summary on nuclei detection and segmentation is presented in [77]. Distance transform based methods have been used to detect seeds (cells) in clustered objects. However, it may not work well for the tightly or densely clustered cells. Endeavors combining geometric and intensity information have been proposed to improve the distance transform methods [78]. Later, to further reduce the false detection, mutual proximity information is exploited to filter out the false seeds [9]. In order to handle cell occlusion/overlap, marker-based watershed approaches [16, 17, 19] are widely utilized to localize and split touching cells. In [20], a variant of marker-controlled watershed generating marker from H-minima transform of nuclei shape is investigated. The H-value is derived from the fitting accuracy between the ellipses and nuclei contours. In [21], an adaptive H-minima transform is proposed in which markers are detected within connected components obtained by inner distance transform. A supervised marker-controlled watershed algorithm is proposed in [14]. In [15], a flood level-based watershed algorithm is reported to split overlapping nuclei on RNAi fluorescent cellular images. A gradient-weighted watershed algorithm [11] followed by a hierarchical merging tree is presented to separate touching cells. In [35], the conventional watershed method is improved by a subregion merging mechanism and a Laplacian-of-Gaussian (LOG) filter on Ki-67 nuclei detection. Kårsnäs *et al.* [79] propose to apply the watershed algorithm and a complement to the distance transform to a pixel level probability map.

Cell detection can also be formulated into a graph cut problem [22]. In [24], cell detection is formulated into a normalized graph cut problem over a weighted graph [80]. Another method applying graph-cut algorithm to an image preprocessed by multiscale LOG filtering is reported in [1]. In [81], nuclei separation is formulated into a multi-reference graph cut problem, which is robust to technical variations introduced by data preparation. Some other graph-based methods can be found in [28], [82]. In [83], markers are derived by a modified ultimate erosion process and a Gaussian mixture model on B-splines is utilized to infer the object shapes and missing object boundaries. Recently, a deep learning-based method [84] is applied to mitosis detection and achieve great performance. However, this framework does not apply to touching cells which are very common in our dataset.

Some recent works exploit the cues in cell structure and shape symmetry to tackle touching cells. Radial voting based methods [2], [34], [3] are proposed to locate the centers of cells with a major assumption on round shaped cells. In [36], image background is removed by a pixel level classifier working on color-texture and touching cells are separated based on concave points and radial symmetry. Fast radial symmetry transform is used for nuclei detection followed by marker-controlled watershed in [85]. A cell splitting method based on ellipse fitting using concave points information is reported in [86]. Su *et al.* [87] propose to learn a classifier to refine the cell detection results obtained by ellipse fitting. Although many methods have been

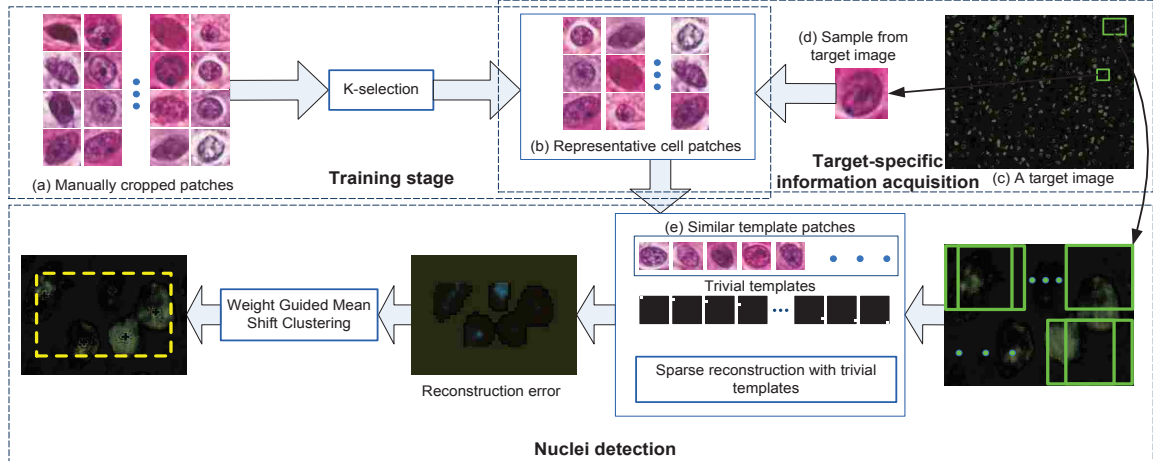


Figure 2.1: An overview of the framework.

proposed, brain tumor cells in histopathological images often exhibit appearance variations and dense overlapping and therefore the accurate cell detection in brain tumor histopathological images remain to be a challenging problem.

Sparse representation has been successfully applied to image classification, object recognition, and image segmentation [88], [89], [90], [91], [92]. Yu *et al.* [93] found that sparse coding with locality constraint (LCC) produces better reconstruction results. However, solving LCC is computationally expensive due to its iterative optimization procedure [94]. An efficient locality-constrained linear coding (LLC) is proposed in [48]. In LLC the desirable properties of sparsity is preserved while locality constraint is treated in favor of sparsity. The problem can be efficiently solved by performing a K-nearest neighbor (KNN) search and then computing an analytical solution to a constrained least square fitting problem.

In this chapter, we propose a novel automatic cell detection algorithm (Figure 2.1) using adaptive dictionary learning and sparse reconstruction with trivial templates. The algorithm consists of the following steps: 1) An initial cell appearance collection, containing single-cell image patches only, is first created from images of different patients at different stages of brain tumors Figure 2.1(a). A representative subset of the collection is extracted by K-selection [47] to form a cell library as shown in Figure 2.1(b). 2) Given a testing image, a target specific dictionary is generated by searching in the library for cells similar to the cells in the testing image. Cosine distance is employed as similarity metric (Figure 2.1(c) and (d)). 3) A sparse representation with trivial templates (Figure 2.1(e)) is computed as an approximation of a sliding window over the target image. A probability map is obtained by comparing the sparsely reconstructed image patch to each sliding window. 4) A weight-guided mean shift clustering is used to generate the final seed detection. The way we generate the dictionary aims to summarize the training data and to use only the relevant information for detection. In other words, the cell library contains a set of prototype appearances of brain tumor cells and only the ones most similar to the cells present in the testing images are used for detection. This can benefit the computational expense. In the sparse optimization, the cell appearance variation is captured by the variation in the dictionary. We apply LLC algorithm to solve the sparse reconstruction problem so that appearance similarity is maximally exploited. Touching cells are handled by the trivial templates.

The rest of this chapter is organized as the following: Section II describes the



proposed framework. Section III evaluate the performance of the proposed system. Section IV concludes this chapter.

## 2.2 Method

### Dictionary Learning

At training stage, we manually crop many image patches of brain tumor cells. Each image patch contains only one cell located in the center of the image patch (Fig. 2.1 (a)). As one can tell, the manually-cropped image patches exhibit an over-complete dictionary, which is neither robust nor efficient. In this article, we propose to exploit the K-selection [47] to select a subset of representative patches to build the cell appearance dictionary. In order to further improve the computational efficiency, we only utilize the patches similar to the testing image patches as the dictionary candidates using a cosine similarity metric [95].

**Representative Patches Extraction by K-Selection:** Each cell patch is represented as a vectorized patch concatenating all the pixel intensities. For  $N$  manually-cropped cell patches  $T = \{\mathbf{t}_i | i = 1, 2, \dots, N\} \in \mathbb{R}^{m \times N}$  ( $\mathbf{t}_i \in \mathbb{R}^m$ ), the K-selection algorithm directly chooses a set of most representative patches to create the dictionary  $B = \{\mathbf{b}_i | i = 1, 2, \dots, K\} \in \mathbb{R}^{m \times K}$  based on locality-constrained sparse representation. The optimization can be formulated as

$$\begin{aligned} \min_{\mathbf{b}_k \in B, \mathbf{x}_i} \sum_{i=1}^N \|\mathbf{t}_i - \sum_{k=1}^K \mathbf{b}_k x_{ik}\|^2 + \lambda \|\mathbf{d}_i \odot \mathbf{x}_i\|^2, \\ \text{s.t. } \mathbf{1}^T \mathbf{x}_i = 1, \quad \forall i, \end{aligned} \quad (2.1)$$

where  $\mathbf{b}_k$  is the  $k$ -th basis patch selected from the original template pool,  $\mathbf{x}_i$  is the representation coefficient that is sparse, and  $\mathbf{d}_i$  is the distance between  $\mathbf{t}_i$  and the basis vectors. The last term in (2.1) models the locality constraint, which encourages each patch to be represented by its local neighbors. The constraint ensures shift invariance.

Equation (2.1) can be optimized by alternatively updating  $B$  or  $\{\mathbf{x}_i\}$  by fixing the other. The  $B$  is updated using a projection-based gradient descent method. Within each iteration, we choose patch  $t_l$  to replace basis  $b_n$ :

$$\mathbf{t}_l^* = \arg \max_{t_l} \frac{-\nabla f_n(\mathbf{t}_l - \mathbf{b}_n)^T}{\|-\nabla f_n\|_2 \|\mathbf{t}_l - \mathbf{b}_n\|_2}, \quad (2.2)$$

where  $\nabla f_n$  is the gradient of cost function (2.1) with respect to basis  $\mathbf{b}_n$ . We accept  $\mathbf{t}_l^*$  if the replacement reduces the value of the cost function, which corresponds to the direction that has the largest correlation with the negative gradient direction. The coefficients  $\{\mathbf{x}_i\}$  in (2.1) are calculated by locality-constrained linear coding in [48]. Note that K-selection does not assume that the data is low-rank. For each patch, only a small fraction of all the patches are used during the optimization procedure. These characteristics are different from the selection-based dictionary learning methods in [49, 50]. Compared to K-SVD [96], K-selection is a selection based method with locality constraint, and it guarantees that similar patches will obtain similar sparse codes without losing discriminative powers. Therefore, the selected patches can better represent all the training image patches.

**Testing Image Specific Dictionary Generation:** Given a testing image, we propose to choose a subset of cell patches in the training dictionary for the subsequent sparse coding. Instead of using the entire learned dictionary, this step can reduce the computational complexity. The *Local steering kernel* (LSK) is used as local features

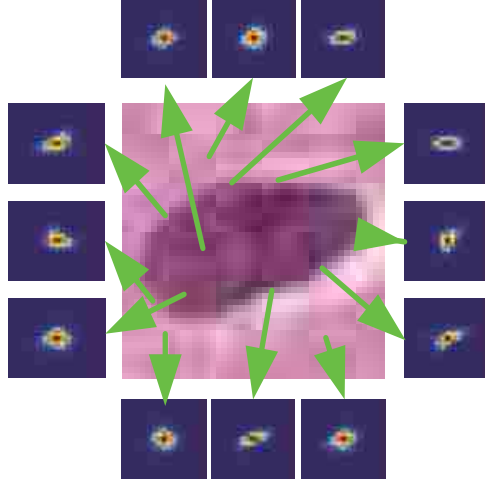


Figure 2.2: The local image structure is encoded by LSK.

to represent each image patch [95]. Matrix cosine similarity [97] is used to measure the similarity between the testing image patch and the learned dictionary bases. The LSK-based feature descriptor measures the local similarity of a pixel to its neighbors by estimating the shape and size of a canonical kernel. This estimation is obtained by analyzing the gradients based on pixel intensities [98]. The canonical kernel  $K(\cdot)$  is modeled by a radially symmetric function:

$$K(\mathbf{x}_l - \mathbf{x}; \mathbf{H}_l) = \frac{K(\mathbf{H}_l^{-1})(\mathbf{x}_l - \mathbf{x})}{\det(\mathbf{H}_l)}, \quad (2.3)$$

$$\mathbf{H}_l = h\mathbf{C}_l^{-\frac{1}{2}} \in \mathbb{R}^{(2 \times 2)}, \quad (2.4)$$

where  $l = 1, \dots, P^2$ ,  $\mathbf{x}_l$  represents pixel location in a local window ( $5 \times 5$ ) centered at  $\mathbf{x}$ ,  $P^2$  is the number of pixels in this window, and  $\mathbf{C}_l$  is a covariance matrix estimated from the pixel intensity in the window. The shape and size of the local kernel is described by the computed steering matrix  $\mathbf{H}_l$ . The local image structure can be captured by the shape and size of such local kernel as shown in Fig. 2.2. A Gaussian function is chosen as the kernel:

$$K(\mathbf{x}_l - \mathbf{x}; \mathbf{H}_l) = \frac{\sqrt{\det(\mathbf{C}_l)}}{2\pi h^2} \exp\left(-\frac{(\mathbf{x}_l - \mathbf{x})^T \mathbf{C}_l (\mathbf{x}_l - \mathbf{x})}{2h^2}\right). \quad (2.5)$$

Because cells often exhibit contrast variations, to make the algorithm robust to contrast variation, a normalized LSK is computed:

$$W_j(\mathbf{x}_l - \mathbf{x}) = \frac{K_j(\mathbf{x}_l - \mathbf{x}; \mathbf{H}_l)}{\sum_{l=1}^{P^2} K_j(\mathbf{x}_l - \mathbf{x}; \mathbf{H}_l)}, \quad \begin{cases} j = 1, \dots, n, \\ l = 1, \dots, P^2, \end{cases} \quad (2.6)$$

where  $n$  is the number of locations where the LSK are computed. We calculate the LSKs by applying a sliding window with spacing size 3 to the sampling patch centered at each pixel in the entire image. Principal component analysis (PCA) is then applied

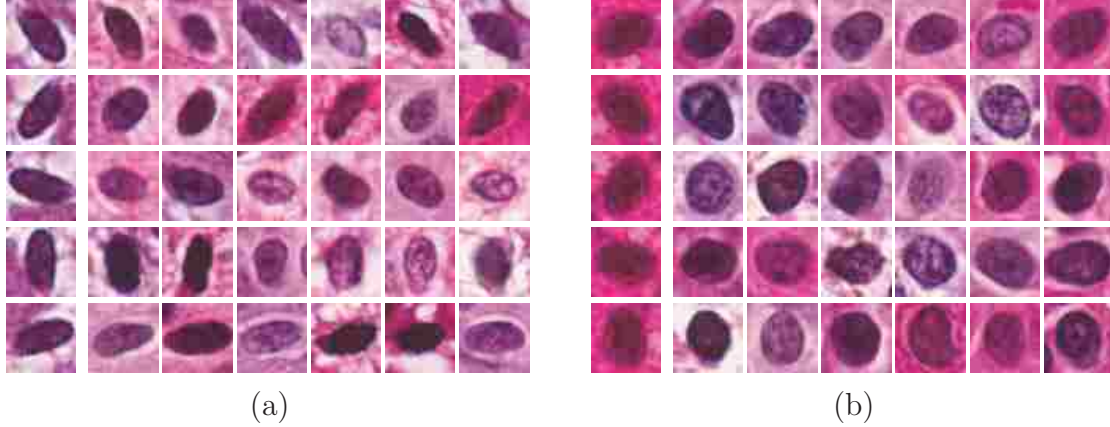


Figure 2.3: Adaptive dictionary generation using two sample patches.

to extract the low dimensional feature descriptions of the local steering kernels for each image patch. Cosine similarity:

$$D_{cos} = \frac{\mathbf{v}_i^T \mathbf{v}_j}{\|\mathbf{v}_i\| \|\mathbf{v}_j\|}, \quad (2.7)$$

is used to measure the similarity between the low dimensional descriptions. The reason for using cosine similarity is that pathologic images could have various contrastness due to unstable staining, and cosine similarity is proven to be robust to contrast change [95].

To handle cell rotation, the sample patch is rotated in different directions, and for each rotation a set of most similar cell templates are selected to be the bases in the dictionary. Fig. 2.3 shows two sample dictionaries given two query cell patches. Each query sample is rotated in 5 orientations as shown in the first column in Fig. 2.3(a) and (b). The first column in each panel shows the rotated versions of a sample patch. Each row of the other columns shows the retrieved relevant patches. For ease of illustration we show only 6 retrieved patches for each rotated version.

### Cell Detection via Sparse Representation with Trivial Templates

In this section, we present the proposed cell detection algorithm based on sparse reconstruction with trivial templates handling touching and overlapping cells and the probability map-based mean shift. A probability map is first generated with sparse reconstruction by running a sliding window to the entire testing image, where the reconstruction errors indicate the probabilities of the presence of cells. The final detection results are obtained by performing the weight-guided mean shift clustering [99].

**Probability Map Generation via Sparse Reconstruction with Trivial Templates:** Following the idea in [100, 101], we assume that cells with similar appearances approximately lie in the same low dimensional subspace. Therefore, a sliding window aligned to a cell should approximately lie in the subspace defined by the the dictionary generated by the method described in subsection 2.2. Given a learned dictionary  $\mathbf{B} \in \mathbb{R}^{m \times q}$ , a sliding window  $\mathbf{p}_{ij}$  aligned to a cell at location  $(i, j)$  can be represented linearly by  $\mathbf{B}$ :

$$\mathbf{p}_{ij} \approx \mathbf{B}\mathbf{c} = c_1 \mathbf{b}_1 + c_2 \mathbf{b}_2 + \dots + c_q \mathbf{b}_q. \quad (2.8)$$

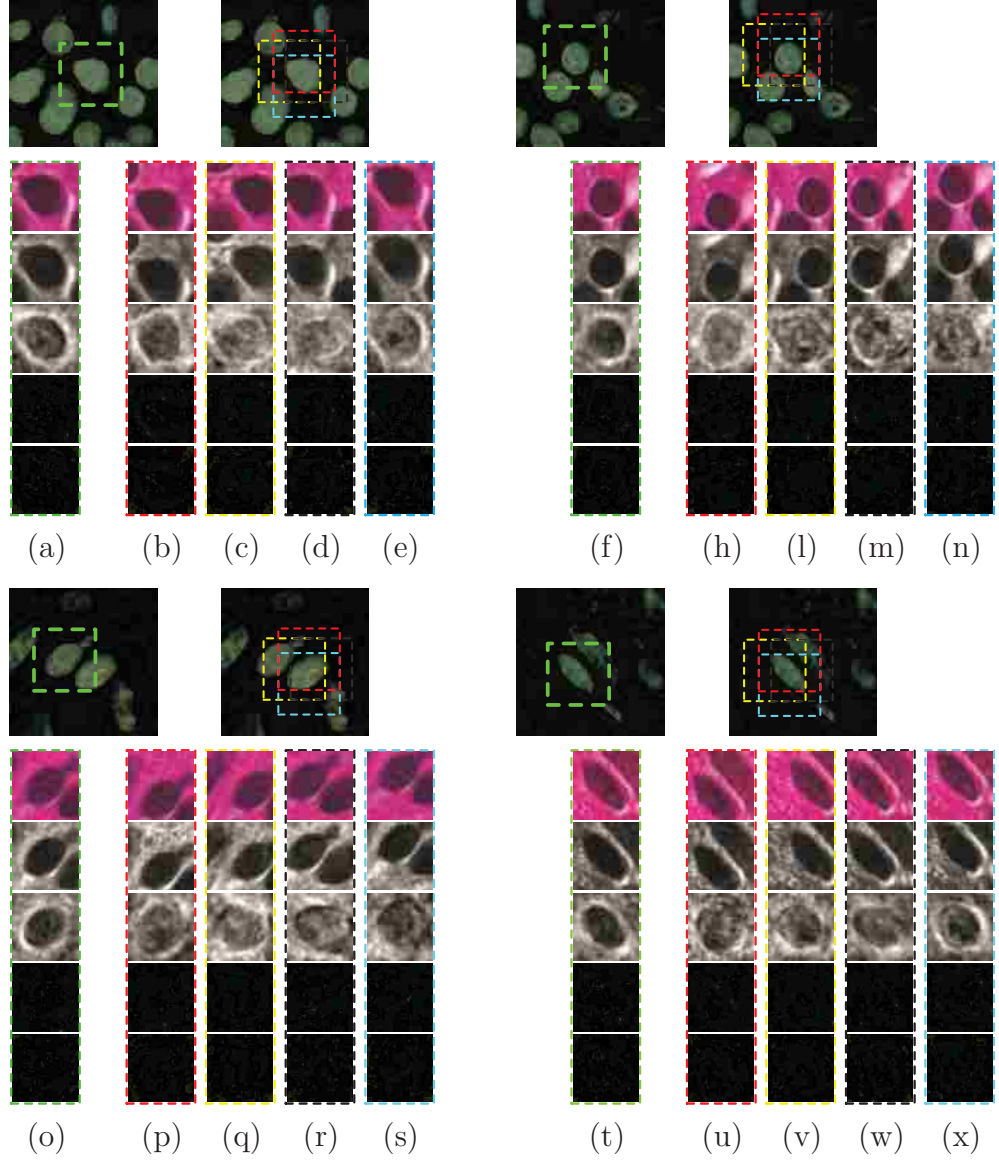


Figure 2.4: Reconstruction results and errors of four cells.

For sliding windows not aligning to a cell, equation 2.8 does not hold. To differentiate the tumor cells from background, we propose to measure how well a sliding window can be represented by a linear combination of the atom patches from the dictionary by:

$$\epsilon_{rec} = \|\mathbf{p}_{ij} - \mathbf{B}\mathbf{c}\|, \quad (2.9)$$

where  $\epsilon_{rec}$  is the reconstruction error and  $\mathbf{c}$  is the reconstruction coefficient. This coefficient can be computed by sparse optimization:

$$\begin{aligned} \min_{\mathbf{c}} \|\mathbf{p}_{ij} - \mathbf{B}\mathbf{c}\|^2 + \lambda \|\mathbf{d} \odot \mathbf{c}\|, \\ s.t. \mathbf{1}^T \mathbf{c} = 1, \end{aligned} \quad (2.10)$$

where  $\mathbf{d}$  is distance between the test patch  $\mathbf{p}_{ij}$  and each dictionary atom, and  $\odot$  denotes element-wise multiplication. The second term in equation 2.10 enforces the

encoding to use only the dictionary atoms near to  $\mathbf{p}_{ij}$ . Intuitively, an input patch containing a cell in its central area can be sparsely reconstructed with relatively small reconstruction error, while a patch that does not have a cell in its center should have relatively large sparse reconstruction error. This is because such patches do not lie in the subspace spanned by the dictionary. To achieve fast encoding, we choose the approximated optimization algorithm presented in [48].

The above formulation deals with single cells with appearance variation well. However, in histopathologic images it is common that cells appear in touching or overlapping. In such case, the appearance of a test patch is significantly different from the atom patches in the dictionary. Thus equation 2.8 needs to be modified into:

$$\mathbf{p}_{ij} \approx \mathbf{B}\mathbf{c} + \mathbf{e}, \quad (2.11)$$

where  $\mathbf{e}$  is an error term used to model the touching part. Equation 2.11 can be rewritten as:

$$\mathbf{p}_{ij} \approx \tilde{\mathbf{B}}\tilde{\mathbf{c}} = [\mathbf{B} \ \mathbf{I}] \begin{bmatrix} \mathbf{c} \\ \mathbf{e} \end{bmatrix}, \quad (2.12)$$

where  $\mathbf{I}$  is called trivial template, and it is an identity matrix of dimension  $m$ . Accordingly equation 2.10 is modified into:

$$\begin{aligned} \min_{\tilde{\mathbf{c}}} \|\mathbf{p}_{ij} - \tilde{\mathbf{B}}\tilde{\mathbf{c}}\|^2 + \lambda\|\mathbf{d} \odot \mathbf{c}\|, \\ \text{s.t. } \mathbf{1}^T \tilde{\mathbf{c}} = 1, \end{aligned} \quad (2.13)$$

where the first term incorporates the trivial templates to model the touching cells and the second term enforces that only the most similar dictionary atoms are used for the sparse reconstruction. This is different from [88, 101] that do not incorporate locality constraint. To solve the locality-constrained sparse optimization for a given input patch, we first perform a KNN search in the dictionary excluding the trivial templates. The selected nearest neighbor bases together with the trivial templates form a much smaller local coordinate. Next, we solve the sparse reconstruction problem with least square-style minimization. We demonstrate the reconstruction results of touching cells with or without trivial template in Fig. 2.5. Two sliding windows aligned to cells touching with other cells are shown in Figure 2.5(a). The reconstructed patches using only the dictionary patches are shown in Figure 2.5(b). Figure 2.5(c) shows reconstructed patch with trivial templates modeling the touching parts. A Visualization of the first term and the second term (error) in Equation 2.11 is displayed in Figure 2.5(d). The upper ones are the clean images and the bottom ones are visualization of the error terms. As we can see that the reconstructions in Figure 2.5(b) without trivial templates have higher level of noise and weaker edges, and the reconstructions in Figure 2.5(c) are very similar to the original image. Compared to the original patches in Figure 2.5(a), it is clear that the clean image in Figure 2.5(d) shows the cell in the central region of Figure 2.5(a), and error term shows the touching cells in the marginal regions. This is due to the contribution of the trivial templates.

The reconstruction error  $\epsilon_{rec}$  of the sliding window forms the probability map indicating the probability of occurrence of a cell. We justify our idea in Fig. 2.4. Reconstruction results and error of 20 sliding windows from two test images are presented in the quadrants. In each quadrant, the test image is shown on the top and the sliding windows are shown below in columns. The sliding window in green box, *e.g.*, Fig. 2.4(a), is aligned to a cell with presence of some parts of other cells.

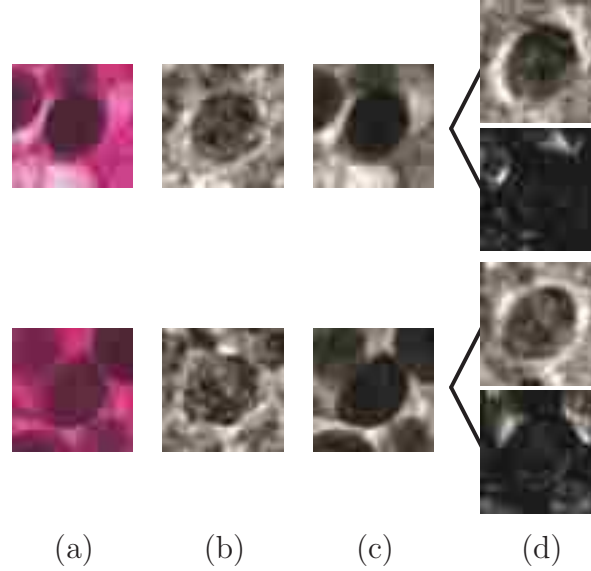


Figure 2.5: Sparse reconstruction with trivial template modeling the touching cells.

The rest are windows off the aligned positions. In each column the first row shows the sliding window. The second row shows the results of the sparse reconstruction with trivial templates. The third row shows the reconstruction results with the parts from other cells being removed. The fourth row shows the reconstruction error. The fifth row shows the spatial kernel weighted reconstruction errors. Our idea can be justified by comparing the reconstruction error of the sliding windows aligned to cells to those off the aligned positions. A more apparent observation is that the clean reconstruction in the third row shows different reconstruction patterns for the aligned and unaligned windows. The reconstructions of the former ones show a single cell with appearance similar to the original cell. However the reconstructions of the latter ones show severe corruptions. This is because the unaligned sliding windows do not lie in the subspace spanned by the dictionary patches. To optimize equation 2.13 more weight concentrates on the trivial templates, therefore the error term in equation 2.11 is larger. Such difference can also be found in the reconstruction error shown in the fourth row. As can be seen the unaligned patches have denser or higher level of reconstruction errors.

**Spatial Kernel Weighted Probability Map:** One observation on the pattern of the reconstruction error is that the errors of the sliding windows aligned to a cell have different concentration patterns than those of the ones off the aligned positions. In other words, the aligned windows have lower concentration of error in the central region of the window, while the unaligned ones tend to have significant concentration of error in the central region. This is because the dictionary patches all have a single cell in the window center and they are good at representing sliding windows aligned to cells. Based on this observation, we propose to weigh the reconstruction errors in the central region more in computing the probability map. We introduce a bell-shape kernel to weigh the errors in central regions more and the errors in marginal regions less. In such way the reconstruction error of the aligned windows can be relatively reduced and those of the unaligned ones can be relatively increased. Therefore, the robustness of the algorithm is enhanced. We demonstrate the effect of spatial weighting in Fig. 2.4. We consider only the sliding windows shown in Fig. 2.4 as an example. The benefit of spatial kernel is measured by the increase of the relative difference between the reconstruction errors of the aligned sliding windows

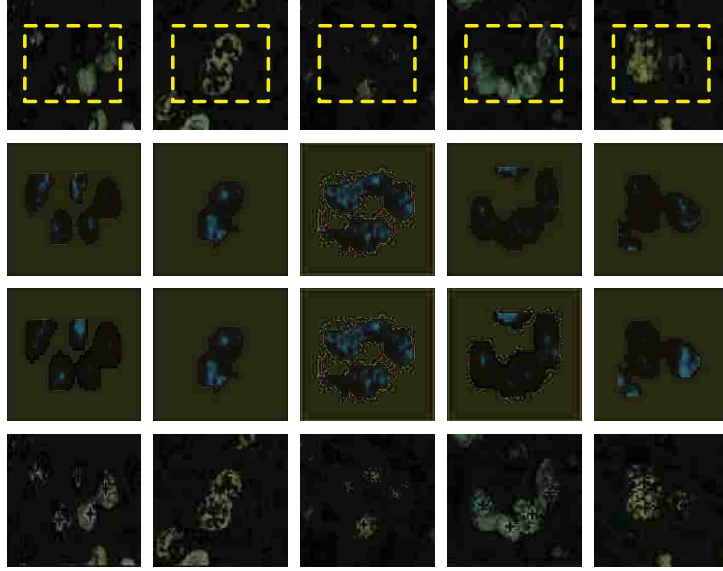


Figure 2.6: Probability maps and detection results.

and their corresponding unaligned windows. The relative difference is defined by:

$$diff_{rel} = \frac{e_{algn} - \bar{e}_{off}}{\bar{e}_{off}}, \quad (2.14)$$

where  $e_{algn}$  denotes the reconstruction error of the aligned window shown in the forth row of the first column in each quadrant of Fig. 2.4, and  $\bar{e}_{off}$  represents the average of the reconstruction error of the 4 unaligned windows shown in the forth row of each quadrant. Such relative difference is increased for the four cells by 5%, 3%, and 1%, and 8% when spatial kernel is used. The weighted reconstruction errors are shown in the fifth row in each quadrant of Fig. 2.4. The benefit also pronounces itself in Fig. 2.6. The first row shows the original test images. Due to the size of the sliding window, only the region inside the yellow boxes are considered for scanning. The second row are the probability maps generated by sparse representation with trivial templates but without spatial weighting. The third row are the probability maps generated by the proposed method. Compared to the second row, the test patches in the last two have better probability map with pronounced local peaks in the cell centers. This is due to the spatial kernel. The forth row are the detection results generated by the weight-guided mean shift clustering based on the probability maps in the third row. For the experiment, we use Gaussian kernel with  $\sigma = 8$  pixel distance.

To improve the efficiency of the sliding window mechanism, we preprocess the images to filter out the background region using edge preserving smoothing [102] followed by Otsu's adaptive thresholding. Only the foreground region is scanned.

**Local Maxima Detection Based on Weight-guided Mean Shift Clustering:** To generate the final point detection from the probability map, we apply weight-guided mean shift clustering [99] to find the local maxima:

$$\hat{f}_{z,K}(\mathbf{x}) = \frac{c_{k,d}}{nz^d} \sum_{i=1}^n w_i k\left(\left\|\frac{\mathbf{x} - \mathbf{x}_i}{z}\right\|^2\right), \quad (2.15)$$

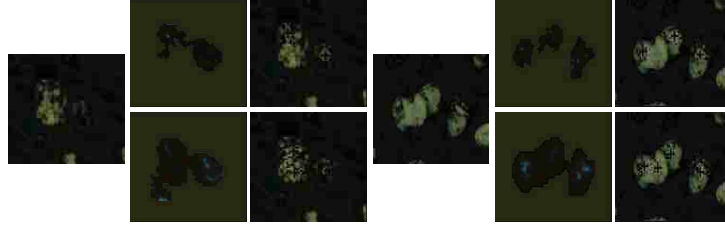


Figure 2.7: Effect of the trivial templates.

where  $\frac{c_{k,d}}{nz^d}$  is constant to make sure the density function sums to 1, and  $z$  denotes the bandwidth, and  $w_i$  is the weight of point  $i$ , and  $k(\cdot)$  is kernel profile defined by kernel functions (*i.e.*, Gaussian kernel or Epanechnikov kernel). The mean shift vector is:

$$\mathbf{m} = \frac{\sum_{i=1}^n w_i \mathbf{x}_i g\left(\left\|\frac{\mathbf{x}-\mathbf{x}_i}{z}\right\|^2\right)}{\sum_{i=1}^n w_i g\left(\left\|\frac{\mathbf{x}-\mathbf{x}_i}{z}\right\|^2\right)} - \mathbf{x}, \quad (2.16)$$

where  $g(\cdot)$  is the derivative of the kernel profile  $k(\cdot)$ . Several randomly picked examples are shown in Fig. 2.6. As can be tell, both touching and non-touching cells are correctly detected.

### 2.3 Experimental Results

We have conducted our experiment based on a data set containing 59 brain tumor images. The images are captured at 40x magnification. 27 images are randomly selected as training images from which 2000 patches with a centralized single cell are manually cropped.  $K = 1400$  of the 2000 patches are picked out by K-selection described in Section 2.2. At least 2000 cells from 32 images are used for testing. The whole algorithm is implemented in MATLAB and run on a work station with 3.3GHz i3 CPU and 16GB memory. Patches with size  $45 \times 45$  are cropped. The parameters in equation (2.3) are set as  $P = 5$ ,  $h = 2$ , and in equations (2.1) and (2.10), the  $\lambda$  is chosen  $10^{-4}$ . In equation (2.15), the  $h$  is selected from  $9 \sim 12$  based on the average size of cells on one specific image.

We first demonstrate the effect of the trivial templates on cell detection. Fig. 2.7 shows the probability map and detection results of two original images containing touching cells. The first row presents the results without trivial templates and the second row is the results with trivial templates. As can be seen in the probability maps, without trivial templates, some cells significantly touching with others tend to be overlooked due to too large reconstruction error. Thus false negatives occur. We also have quantitatively compared the detection performance with and without the trivial templates, and the comparison confirms that the trivial template does help to improve the performance. The results are shown in Table 2.1 and 2.2. The definition of the performance metrics is presented in the following paragraphs.

We evaluate the performance of the proposed algorithm by comparing it with four state-of-the-art cell detection methods, *i.e.*, Laplacian-of-Gaussian (LoG) [1], Iterative radial voting (IRV) [2], and ITCN [4], and Single-pass voting (SPV) [3], through both qualitative analysis and quantitative analysis. In Fig. 2.8, thousands of cells with various shapes and clustering are correctly detected. A qualitative comparison between our method and the four existing methods is displayed in Fig. 2.9. It can be seen that LoG is sensitive to heterogenous intensity of the objects (Fig. 2.9 (a) and (b)). Besides, both LoG and IRV tend to produce false positive detection on



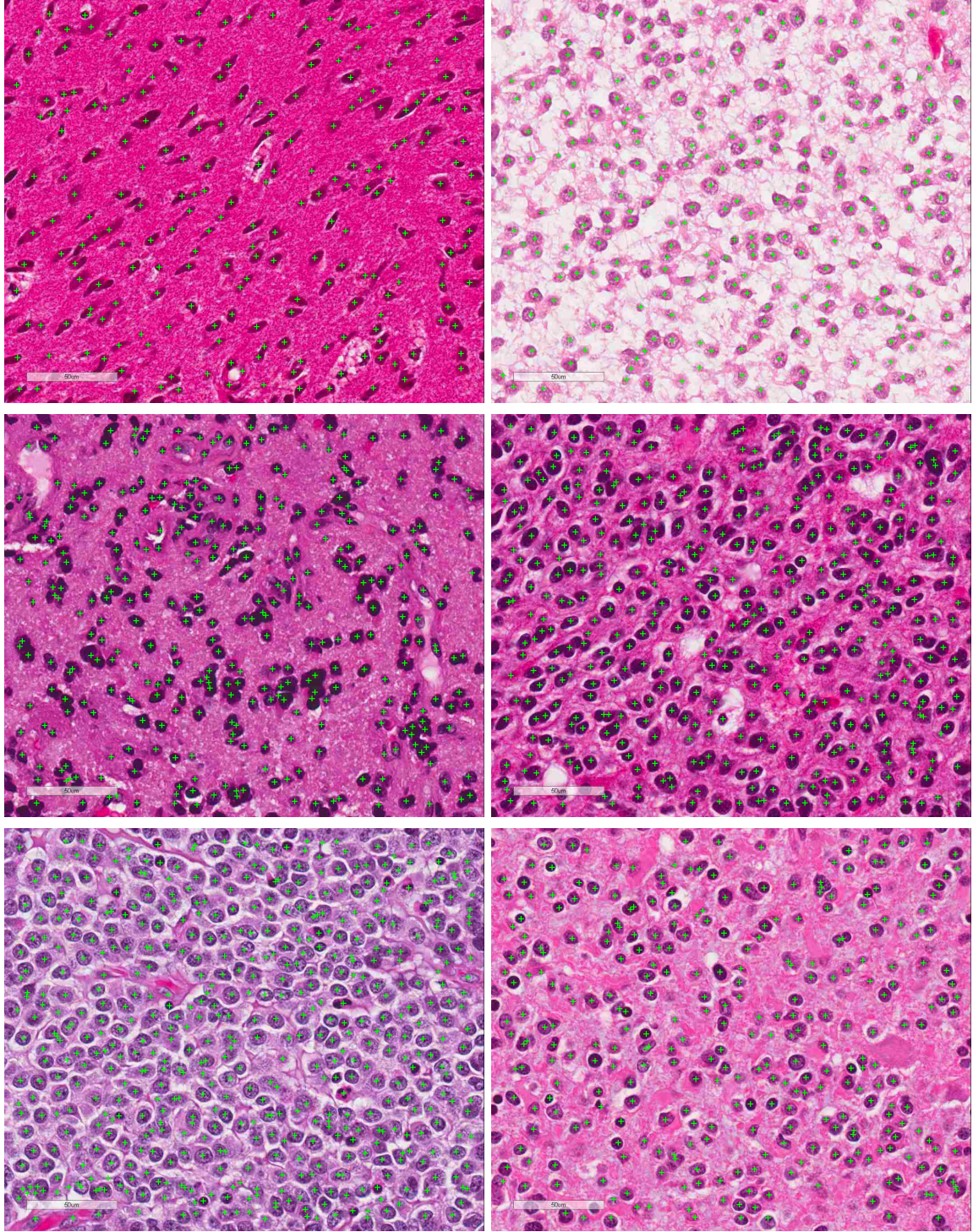


Figure 2.8: Detection results of whole target images.

elongated cells (Fig. 2.9 (c)-(f)). In contrast to LoG and IRV, although ITCN is more robust to shape variation and inhomogeneous intensity but it fails to detect the cells with lighter intensity touching with a darker one (Fig. 2.9 (a), (b) and (e)). Performance of SPV is close to our method, but it is not robust enough to elongated

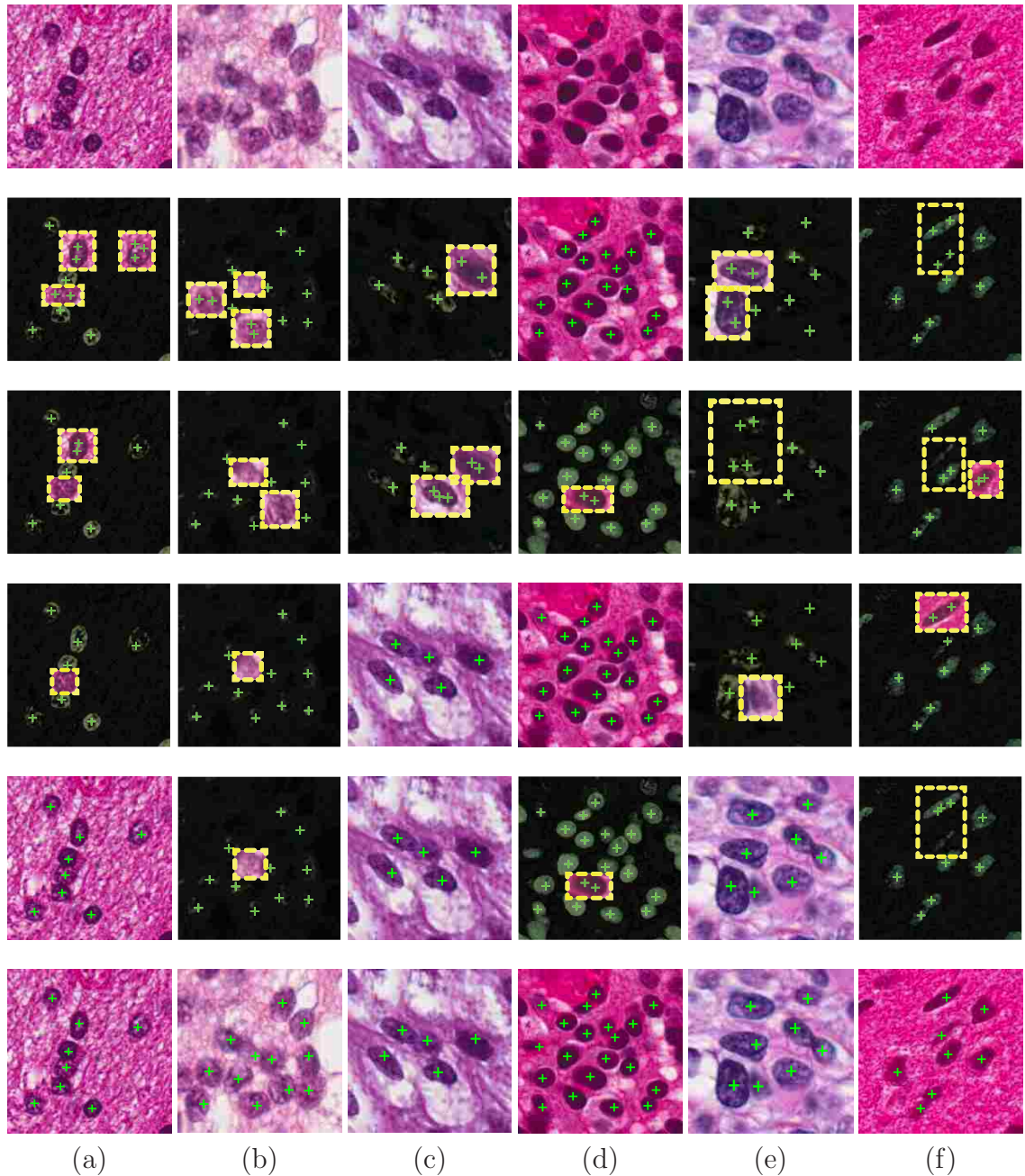


Figure 2.9: Qualitative comparison with LoG [1], IRV [2], and ITCN [4], and SPV [3].

shapes. Our algorithm is robust to shape variation and/or cell clustering. This is due to: 1) The information of various shapes is captured by the cell dictionary and is encoded to represent the cells with different shapes; 2) The touching case can be handled by the sparse representation with trivial templates modeling the touching corners.

For quantitative comparison, we measure the pixel-wise Euclidean distance between the manually annotated cell centers and the seeds detected by the algorithms. In this assessment, we only consider the correctly detected seeds that are algorithm-

Table 2.1: Comparative performance evaluation by seed offset.

Algorithms	Mean	Variance	Min	Max
LoG [1]	3.13	3.14	0	8
IRV [2]	2.85	3.09	0	8
ITCN [4]	3.04	4.02	0	8
SPV [3]	<b>2.7</b>	2.97	0.25	<b>7.9</b>
SR no Triv. Templ.	3.06	3.10	0	8
SR with Triv. Templ.	2.88	<b>2.64</b>	0	8

Table 2.2: Comparative performance evaluation for a circle with radius of 8 pixels

Algorithms	UR	OR	ER	P	R	F1
LoG [1]	0.15	0.3	0.8	0.94	0.84	0.89
IRV [2]	0.15	0.07	0.76	0.95	0.83	0.88
ITCN [4]	0.22	<b>0.01</b>	0.77	0.99	0.77	0.87
SPV [3]	0.1	0.06	0.86	0.98	0.89	0.93
SR no Triv. Templ.	0.09	0.05	0.91	0.99	0.91	0.95
SR with Triv. Templ.	<b>0.07</b>	0.04	<b>0.92</b>	0.99	<b>0.93</b>	<b>0.96</b>

produced seeds within 8-pixel distance to the ground truth cell centers. The results are listed in Table 2.1. It can be seen that the seed deviation achieved by our method has the smallest variance and a mean error competitive with the smallest one (SPV). To show the effect of trivial templates we also include the performance of an algorithm based on sparse representation but without the trivial templates in the table. We do observe some performance drop with such algorithm. To evaluate our algorithm comprehensively, we define a set of metrics including missing rate ( $MR$ ), over-detection rate ( $OR$ ), effective rate ( $ER$ ), precision, recall and  $F_1$  score.  $MR$  means no seed is detected within 8-pixel distance to a ground truth seed.  $OR$  is the portion of the ground truth seeds that have multiple detected seeds within a circle of 12-pixel distance.  $ER$  is the ratio of the number of the detected seeds over the number of the ground truth seeds. Precision ( $P$ ), recall ( $R$ ) and  $F_1$  score are defined as  $P = \frac{TP}{TP+FP}$ ,  $R = \frac{TP}{TP+FN}$ , and  $F_1 = \frac{2*P*R}{P+R}$ , where  $TP$ ,  $FP$  and  $FN$  denote true positive, false positive and false negative, respectively. In our experiment, true positive is defined as a detected seed that is within 8-pixel distance to a ground truth and there is no other seeds in a circular region with a radius  $r = 12$  pixels around this ground truth. False positive is asserted if multiple seeds are detected within a circular neighborhood with  $r = 12$  pixels around a ground truth seed. A false negative is counted if no seed is detected inside a circular neighborhood with  $r = 8$  pixels around a ground truth seed. The comparison results are shown in Table 2.2. It can be seen that the proposed sparse representation with trivial templates outperforms all other methods except for over detection rate.

Finally, we evaluate the effect of the number of nearest neighbors on the detection performance. We show the precision, recall, and  $F_1$  score as functions of the number of local neighbors used for sparse reconstruction. We experimented with a set of  $\{10, 25, 50, 75, 100\}$  nearest neighbors. As the increase of the neighbors involved in the sparse reconstruction, the detection performance is improved. The results are shown

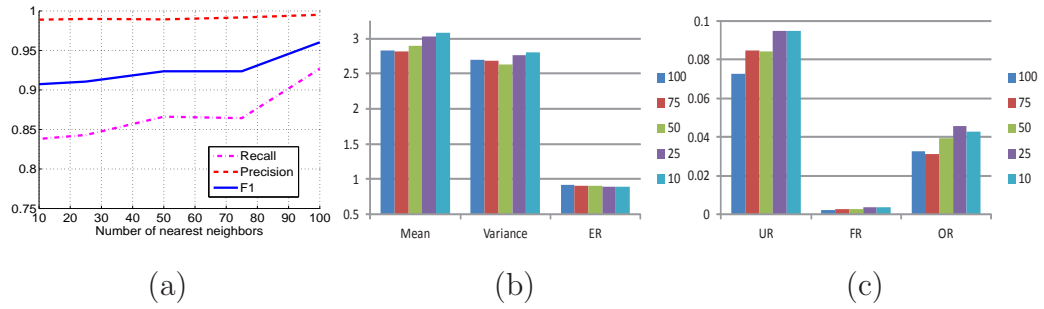


Figure 2.10: Effect of the number of local neighbors on the detection performance.

in Fig. 2.10(a). Other metrics described above are shown in the bar plots in Fig. 2.10(b) and (c). As we can see that as increase of the number of neighbors used, the three metrics all improve. This is due to the fact that the more cell templates are involved the more variation information is captured. Therefore more cells in the target image can be correctly detected.

### Chapter 3 Conclusion and Future Work

Biology researches and cancer clinical diagnosis usually own much of their power to nuclei/cell detection and quantification in microscopic images. In this thesis we have presented two automatic nuclei/cell detection algorithms. One is designed for microscopic skeletal muscle fibers. The other is developed for brain tumor histopathological images.

In the first algorithm Our approach tackles the challenges in splitting clusters consisting of myonuclei with diverse shapes and sizes using a robust ellipse fitting based on heteroscedastic errors-in-variables (HEIV) regression, sample and feature selection by two-stage sparse optimization model, and learning based refinement and mean-shift clustering using geodesic inner-distance. The proposed algorithm is resilient to the variations in nuclear shapes and sizes. The experimental results demonstrate that this algorithm outperforms many existing state-of-the-art approaches. Previously, it is very common for a biology lab to analyze hundreds of isolated fibers from various muscle perturbations, requiring an incredible amount of time- and man-power for accurate quantification. This automatic approach is an exciting endeavor that can efficiently and accurately quantify the myofiber adaptation.

In the second part, we have introduced an automatic cell detection algorithm for locating brain tumor cells in histopathological images. The algorithm splits the touching cells through computing the reconstruction error of sparse reconstruction with trivial templates. An image patch aligned to a cell usually can be reconstructed with the minimal reconstruction error (producing a local maxima in the probability map). Cell appearance variation among images are tackled jointly by exploiting target cell specific information and the appearance variation in the cell appearance dictionary. The proposed approach works well for different images containing cells with large variations in appearance, shape and scale. The comparative experiments indicate that our method outperforms the other four state of the arts. The proposed framework can be applied to cell detection on other pathological images such as lung tumor images and breast cancer images. The only change is to rebuild a cell dictionary based on some sample images from a particular disease and choose an appropriate patch size. We will perform experiments on other applications in the future.

## Bibliography

- [1] Y. Al-Kofahi, W. Lassoued, W. Lee, and B. Roysam, "Improved automatic detection and segmentation of cell nuclei in histopathology images," *IEEE Trans. on Biomedical Engineering*, vol. 57, no. 4, pp. 841–852, apr. 2010.
- [2] B. Parvin, Q. Yang, J. Han, H. Chang, B. Rydberg, and M. H. Barcellos-Hoff, "Iterative voting for inference of structural saliency and characterization of subcellular events," *IEEE Trans. on Image Processing*, vol. 16, no. 3, pp. 615–623, 2007.
- [3] X. Qi, F. Xing, D. Foran, and L. Yang, "Robust segmentation of overlapping cells in histopathology specimens using parallel seed detection and repulsive level set," *IEEE Trans. on Biomedical Engineering*, vol. 59, no. 3, pp. 754–765, mar. 2012.
- [4] J. Byun, M. R. Verardo, B. Sumengen, G. P. Lewis, B. Manjunath, and S. K. Fisher, "Automated tool for the detection of cell nuclei in digital microscopic images: application to retinal images," *Mol Vis*, vol. 12, pp. 949–960, 2006.
- [5] J. J. McCarthy, J. Mula, M. Miyazaki, R. Erfani, K. Garrison, A. B. Farooqui, R. Srikuea, B. A. Lawson, B. Grimes, C. Keller, G. Van Zant, K. S. Campbell, K. A. Esser, E. E. Dupont-Versteegden, and C. A. Peterson, "Effective fiber hypertrophy in satellite cell-depleted skeletal muscle," *Development*, vol. 138, no. 17, pp. 3657–3666, 2011.
- [6] J. R. Jackson, J. Mula, T. J. Kirby, C. S. Fry, J. D. Lee, M. F. Ubele, K. S. Campbell, J. J. McCarthy, C. A. Peterson, and E. E. Dupont-Versteegden, "Satellite cell depletion does not inhibit adult skeletal muscle regrowth following unloading-induced atrophy," *American Journal of Physiology - Cell Physiology*, vol. 303, no. 8, pp. C854–C861, 2012.
- [7] N. Malpica, C. O. de Solorzano, J. J. Vaquero, A. Santos, I. Vallcorba, J. M. Garcia-Sagredo, and F. del Pozo, "Applying watershed algorithms to the segmentation of clustered nuclei," *Journal of Cytometry*, vol. 28, no. 4, pp. 289–297, Aug. 1997.
- [8] G. Lin, U. Adiga, K. Olson, J. F. Guzowski, C. A. Barnes, and B. Roysam, "A hybrid 3d watershed algorithm incorporating gradient cues and object models for automatic segmentation of nuclei in confocal image stacks," *Journal of Cytometry*, vol. 56A, no. 1, pp. 23–36, 2003.
- [9] H. Ancin, B. Roysam, T. Dufresne, M. Chestnut, G. Ridder, D. Szarowski, and J. Turner, "Advances in automated 3-d image analysis of cell populations imaged by confocal microscopy," *Journal of Cytometry*, vol. 25, no. 3, pp. 22–234, 1996.
- [10] L. Vincent and P. Soille, "Watersheds in digital spaces: an efficient algorithm based on immersion simulations," *IEEE Trans. on Pattern Analysis and Machine Intelligence (TPAMI)*, vol. 13, no. 6, pp. 583–598, 1991.
- [11] G. Lin, M. K. Chawla, K. Olson, C. A. Barnes, J. F. Guzowski, C. Bjornsson, W. Shain, and B. Roysam, "A multi-model approach to simultaneous segmentation and classification of heterogeneous populations of cell nuclei in 3d confocal microscope images," *Cytometry Part A*, vol. 71A, no. 9, pp. 724–736, 2007.

- [12] G. Lin, U. Adiga, K. Olson, J. F. Guzowski, C. A. Barnes, and B. Roysam, "A hybrid 3d watershed algorithm incorporating gradient cues and object models for automatic segmentation of nuclei in confocal image stacks," *Cytometry Part A*, vol. 56A, no. 1, pp. 23–36, 2003.
- [13] W. Yu, H. K. Lee, S. Hariharan, W. Bu, and S. Ahmed, "Quantitative neurite outgrowth measurement based on image segmentation with topological dependence," *Cytometry Part A*, vol. 75A, no. 4, pp. 289–297, 2009.
- [14] K. Mao, P. Zhao, and P. Tan, "Supervised learning-based cell image segmentation for p53 immunohistochemistry," *IEEE Trans. on Biomedical Engineering*, vol. 53, no. 6, pp. 1153–1163, June 2006.
- [15] P. Yan, X. Zhou, M. Shah, and S. Wong, "Automatic segmentation of high-throughput rna fluorescent cellular images," *IEEE Trans. on Information Technology in Biomedicine*, vol. 12, no. 1, pp. 109–117, January 2008.
- [16] V. Grau, A. U. J. Mewes, M. Alcaniz, R. Kikinis, and S. Warfield, "Improved watershed transform for medical image segmentation using prior information," *IEEE Trans. on Medical Imaging*, vol. 23, no. 4, pp. 447–458, 2004.
- [17] X. Yang, H. Li, and X. Zhou, "Nuclei segmentation using marker-controlled watershed, tracking using mean-shift, and kalman filter in time-lapse microscopy," *IEEE Trans. on Circuits and Systems I: Regular Papers*, vol. 53, no. 11, pp. 2405–2414, 2006.
- [18] L. Yang, O. Tuzel, P. Meer, and D. Foran, "Automatic image analysis of histopathology specimens using concave vertex graph," in *Proc. of the Inter. Conf. on Medical Image Computing and Computer-Assisted Intervention - Part I*, ser. MICCAI, 2008, pp. 833–841.
- [19] O. Schmitt and M. Hasse, "Radial symmetries based decomposition of cell clusters in binary and gray level images," *Journal of Pattern Recognition*, vol. 41, no. 6, pp. 1905–1923, June 2008.
- [20] C. Jung and C. Kim, "Segmenting clustered nuclei using h-minima transform-based marker extraction and contour parameterization," *IEEE Trans. on Biomedical Engineering*, vol. 57, no. 10, pp. 2600–2604, October 2010.
- [21] J. Cheng and J. Rajapakse, "Segmentation of clustered nuclei with shape markers and marking function," *IEEE Trans. on Biomedical Engineering*, vol. 56, no. 3, March 2009.
- [22] V. Kolmogorov and R. Zabih, "What energy functions can be minimized via graph cuts?" *IEEE Trans. on Pattern Analysis and Machine Intelligence (TPAMI)*, vol. 26, no. 2, pp. 147–159, 2004.
- [23] Y. Boykov and G. Funka-Lea, "Graph cuts and efficient n-d image segmentation," *Inter. J. Comput. Vision (IJCV)*, vol. 70, no. 2, pp. 109–131, November 2006.
- [24] E. Bernardis and S. Yu, "Finding dots: Segmentation as popping out regions from boundaries," in *Proc. of IEEE Conf. on Computer Vision and Pattern Recognition (CVPR)*, June 2010, pp. 199–206.

- [25] J. Shi and J. Malik, "Normalized cuts and image segmentation," *IEEE Trans. on Pattern Analysis and Machine Intelligence (TPAMI)*, vol. 22, no. 8, pp. 888–905, 2000.
- [26] Q. Wen, H. Chang, and B. Parvin, "A delaunay triangulation approach for segmenting clumps of nuclei," in *Proc. of IEEE Inter. Symp. on Biomedical Imaging: From Nano to Macro (ISBI)*, 2009, pp. 9–12.
- [27] S. K. Nath, K. Palaniappan, and F. Bunyak, "Cell segmentation using coupled level sets and graph-vertex coloring," in *Proc. of Inter. Conf. on Medical Image Computing and Computer-Assisted Intervention (MICCAI)*, 2006, pp. 101–108.
- [28] G. M. Faustino, M. Gattass, S. Rehen, and C. de Lucena, "Automatic embryonic stem cells detection and counting method in fluorescence microscopy images," in *Proc. of IEEE Inter. Symp. on Biomedical Imaging: From Nano to Macro (ISBI)*, 2009, pp. 799–802.
- [29] C. Chen, H. Li, X. Zhou, and S. Wong, "Constraint factor graph cut-based active contour method for automated cellular image segmentation in rnai screening," *Journal of microscopy*, vol. 230, no. 2, pp. 177–191, 2008.
- [30] Z. Wu, D. Gurari, J. Y. Wong, and M. Betke, "Hierarchical partial matching and segmentation of interacting cells," in *Proc. of Inter. Conf. on Medical Image Computing and Computer-Assisted Intervention (MICCAI)*, 2012, pp. 389–396.
- [31] W. Yu, H. K. Lee, S. Hariharan, W. Bu, and S. Ahmed, "Evolving generalized voronoi diagrams for accurate cellular image segmentation," *Cytometry Part A*, vol. 77, no. 4, pp. 379–386, 2010.
- [32] A. Janowczyk, S. Chandran, R. Singh, D. Sasaroli, G. Coukos, M. D. Feldman, and A. Madabhushi, "High-throughput biomarker segmentation on ovarian cancer tissue microarrays via hierarchical normalized cuts," *IEEE Trans. on Biomedical Engineering*, vol. 59, no. 5, pp. 1240–1252, 2012.
- [33] O. Sertel, B. Dogdas, C. S. Chiu, and M. N. Gurcan, "Microscopic image analysis for quantitative characterization of muscle fiber type composition," *Journal of Computerized Medical Imaging and Graphics*, vol. 35, pp. 616–628, 2011.
- [34] A. Hafiane, F. Bunyak, and K. Palaniappan, "Fuzzy clustering and active contours for histopathology image segmentation and nuclei detection," in *Advanced concepts for intelligent vision systems*, 2008, pp. 903–914.
- [35] H. Cinar Akakin, H. Kong, C. Elkins, J. Hemminger, B. Miller, J. Ming, E. Plocharczyk, R. Roth, W. M., R. Ziegler, G. Lozanski, and M. Gurcan, "Automated detection of cells from immunohistochemically-stained tissues: application to ki-67 nuclei staining," in *Proc. of Medical Imaging 2012: Computer-Aided Diagnosis, SPIE*, vol. 8315, February 2012.
- [36] H. Kong, M. Gurcan, and K. Belkacem-Boussaid, "Partitioning histopathological images: An integrated framework for supervised color-texture segmentation and cell splitting," *IEEE Trans. on Medical Imaging*, vol. 30, no. 9, pp. 1661–1677, September 2011.
- [37] G. Li, T. Liu, J. Nie, L. Guo, J. Malicki, A. Mara, S. A. Holley, W. Xia, and S. T. Wong, "Detection of blob objects in microscopic zebrafish images based on gradient vector diffusion," *Cytometry Part A*, vol. 71, no. 10, pp. 835–845, 2007.



- [38] N. Otsu, "A threshold selection method from gray-level histograms," *IEEE Trans. on Systems, Man and Cybernetics*, vol. 9, no. 1, pp. 62–66, January 1979.
- [39] H. Hariharan, A. Koschan, and M. Abidi, "Multifocus image fusion by establishing focal connectivity," in *Proc. of IEEE Inter. Conf. on Image Processing (ICIP)*, vol. 3, 2007, pp. III–321–III–324.
- [40] F. P. Kuhl and C. R. Giardina, "Elliptic fourier features of a closed contour," *Journal of Computer Graphics and Image Processing*, vol. 18, no. 3, pp. 236–258, 1982.
- [41] F. P. Kuhl, "Elliptical fourier descriptor of a closed contour," *Computer Graphics and Image Processing*, vol. 18, pp. 236–258, 1982.
- [42] A. W. Fitzgibbon, M. Pilu, and R. B. Fisher, "Direct least-squares fitting of ellipses," *IEEE Trans. on Pattern Analysis and Machine Intelligence (TPAMI)*, vol. 21, no. 5, pp. 476–480, 1999.
- [43] Z. Zhang, "Parameter estimation techniques: A tutorial with application to conic fitting," *Image and vision Computing*, vol. 15, no. 1, pp. 59–76, 1997.
- [44] B. Matei and P. Meer, "Reduction of bias in maximum likelihood ellipse fitting," in *Proc. of Inter. Conf. on Pattern Recognition*, vol. 3, 2000, pp. 794–798.
- [45] G. Taubin, "Estimation of planar curves, surfaces, and nonplanar space curves defined by implicit equations with applications to edge and range image segmentation," *IEEE Trans. on Pattern Analysis and Machine Intelligence*, vol. 13, no. 11, pp. 1115–1138, 1991.
- [46] B. Matei and P. Meer, "A general method for errors-in-variables problems in computer vision," in *Proc. of IEEE Conf. on Computer Vision and Pattern Recognition (CVPR)*, vol. 2, 2000, pp. 18–25.
- [47] B. Liu, J. Huang, L. Yang, and C. Kulikowsk, "Robust tracking using local sparse appearance model and k-selection," in *Proc. of IEEE Conf. on Computer Vision and Pattern Recognition (CVPR)*, 2011, pp. 1313–1320.
- [48] J. Wang, J. Yang, K. Yu, F. Lv, T. Huang, and Y. Gong, "Locality-constrained linear coding for image classification," in *Proc. of IEEE Conf. on Computer Vision and Pattern Recognition (CVPR)*, 2010, pp. 3360–3367.
- [49] J. Bien, Y. Xu, and M. W. Mahoney, "Robust subspace segmentation by low-rank representation," *Advances in Neural Information Processing Systems (NIPS)*, pp. 217–225, 2010.
- [50] G. Liu, Z. Lin, and Y. Yu, "Robust subspace segmentation by low-rank representation," *Proc. of Inter. Conf. on Machine Learning (ICML)*, pp. 663–670, 2010.
- [51] J. Liu, S. Ji, and J. Ye, *SLEP: Sparse Learning with Efficient Projections*, Arizona State University, 2009. [Online]. Available: <http://www.public.asu.edu/~jye02/Software/SLEP>
- [52] M. Turk and A. Pentland, "Eigenfaces for recognition," *Journal of Cognitive Neuroscience*, vol. 3, no. 1, pp. 71–86, 1991.

- [53] J. B. Tenenbaum, V. De Silva, and J. C. Langford, "A global geometric framework for nonlinear dimensionality reduction," *Science*, vol. 290, no. 5500, pp. 2319–2323, 2000.
- [54] S. T. Roweis and L. K. Saul, "Nonlinear dimensionality reduction by locally linear embedding," *Science*, vol. 290, no. 5500, pp. 2323–2326, 2000.
- [55] J. Friedman, T. Hastie, and R. Tibshirani, "Additive logistic regression: a statistical view of boosting (with discussion and a rejoinder by the authors)," *The annals of statistics*, vol. 28, no. 2, pp. 337–407, 2000.
- [56] Y. Liang, L. Wang, S. Liao, and B. Zou, "Feature selection via simultaneous sparse approximation for person specific face verification," in *Proc. of IEEE Inter. Conf. on Image Processing (ICIP)*, 2011, pp. 789–792.
- [57] P. A. Mundra and J. C. Rajapakse, "Svm-rfe with relevancy and redundancy criteria for gene selection," in *Pattern Recognition in Bioinformatics*, 2007, pp. 242–252.
- [58] X. He, D. Cai, and P. Niyogi, "Laplacian score for feature selection," *Advances in Neural Information Processing Systems*, vol. 18, p. 507, 2006.
- [59] F. Nie, S. Xiang, Y. Jia, C. Zhang, and S. Yan, "Trace ratio criterion for feature selection," in *Proc. of The 23rd National Conference on Artificial Intelligence*, vol. 2, 2008, pp. 671–676.
- [60] M. Robnik-Šikonja and I. Kononenko, "Theoretical and empirical analysis of relieff and rrelieff," *Machine Learning*, vol. 53, no. 1-2, pp. 23–69, 2003.
- [61] Z. Zhao and H. Liu, "Spectral feature selection for supervised and unsupervised learning," in *Proc. of Inter. Conf. on Machine Learning (ICML)*, 2007, pp. 1151–1157.
- [62] L. Song, A. Smola, A. Gretton, K. M. Borgwardt, and J. Bedo, "Supervised feature selection via dependence estimation," in *the 24th Inter. Conf. on Machine Learning*, 2007, pp. 823–830.
- [63] H. Ling and D. Jacobs, "Shape classification using the inner-distance," *IEEE Trans. on Pattern Analysis and Machine Intelligence (TPAMI)*, vol. 29, no. 2, pp. 286–299, February 2007.
- [64] A. Brack, H. Bildsoe, and S. Hughes, "Evidence that satellite cell decrement contributes to preferential decline in nuclear number from large fibres during murine age-related muscle atrophy," *Journal of Cell Science*, vol. 118, pp. 4813–4821, 2005.
- [65] T. Joachims, *Making Large-Scale SVM Learning Practical*. Advances in Kernel Methods - Support Vector Learning. B. Scholkopf and C. Burges and A. Smola (ed.). MIT-Press, 1999.
- [66] L. Fei-Fei and P. Perona, "A bayesian hierarchical model for learning natural scene categories," in *Proc. of IEEE Conf. on Computer Vision and Pattern Recognition (CVPR)*, vol. 2, 2005, pp. 524–531.
- [67] B. Leibe, A. Leonardis, and B. Schiele, "Combined object categorization and segmentation with an implicit shape model," in *ECCV04 Workshop on Statistical Learning in Computer Vision*, 2004, pp. 17–32.

- [68] S. Lazebnik, C. Schmid, and J. Ponce, “Beyond bags of features: Spatial pyramid matching for recognizing natural scene categories,” in *Proc. of IEEE Conf. on Computer Vision and Pattern Recognition (CVPR)*, vol. 2, 2006, pp. 2169–2178.
- [69] I. Guyon, J. Weston, S. Barnhill, and V. Vapnik, “Gene selection for cancer classification using support vector machines,” *Machine learning*, vol. 46, no. 1-3, pp. 389–422, 2002.
- [70] K.-B. Duan, J. C. Rajapakse, H. Wang, and F. Azuaje, “Multiple svm-rfe for gene selection in cancer classification with expression data,” *IEEE Trans. on NanoBioscience*, vol. 4, no. 3, pp. 228–234, 2005.
- [71] J. Ferlay, I. Soerjomataram, M. Ervik, R. Dikshit, S. Eser, C. Mathers, M. Rebelo, D. M. Parkin, D. Forman, and F. Bray, “Globocan 2012 v1.0, cancer incidence and mortality worldwide: Iarc cancerbase no. 11,” accessed: 07-11-2014. [Online]. Available: <http://globocan.iarc.fr>
- [72] L. S. Hu, L. C. Baxter, K. A. Smith, B. G. Feuerstein, J. P. Karis, J. M. Eschbacher, S. W. Coons, P. Nakaji, R. F. Yeh, J. Debbins, and et al., “Relative cerebral blood volume values to differentiate high-grade glioma recurrence from posttreatment radiation effect: direct correlation between image-guided tissue histopathology and localized dynamic susceptibility-weighted contrast-enhanced perfusion mr imaging measurements,” *American Journal of Neuroradiology*, vol. 30, no. 3, pp. 552–558, 2009.
- [73] C. F. Lucchinetti, B. F. G. Popescu, R. F. Bunyan, N. M. Moll, S. F. Roemer, H. Lassmann, W. Brück, J. E. Parisi, B. W. Scheithauer, C. Giannini, and et al., “Inflammatory cortical demyelination in early multiple sclerosis,” *New England Journal of Medicine*, vol. 365, no. 23, pp. 2188–2197, 2011.
- [74] F. Ghaznavi, A. Evans, A. Madabhushi, and M. Feldman, “Digital imaging in pathology: whole-slide imaging and beyond,” *Annual Review of Pathology: Mechanisms of Disease*, vol. 8, pp. 331–359, 2013.
- [75] S. B. Wharton, E. Maltby, D. A. Jellinek, D. Levy, N. Atkey, S. Hibberd, D. Crimmins, K. Stoeber, and G. H. Williams, “Subtypes of oligodendroglioma defined by 1p, 19q deletions, differ in the proportion of apoptotic cells but not in replication-licensed non-proliferating cells,” *Acta neuropathologica*, vol. 113, no. 2, pp. 119–127, 2007.
- [76] D. Scheie, M. Cvancarova, S. Mørk, K. Skullerud, P. A. Andresen, I. Benestad, E. Helseth, T. Meling, and K. Beiske, “Can morphology predict 1p/19q loss in oligodendroglial tumours?” *Histopathology*, vol. 53, no. 5, pp. 578–587, 2008.
- [77] M. Veta, J. Pluim, P. van Diest, and M. Viergever, “Breast cancer histopathology image analysis: A review,” *IEEE Transactions on Biomedical Engineering*, vol. 61, no. 5, pp. 1400–1411, May 2014.
- [78] N. Malpica, C. Ortiz de Solorzano, J. J. Vaquero, A. Santos, I. Vallcorba, J. M. Garcia-Sagredo, and F. d. Pozo, “Applying watershed algorithms to the segmentation of clustered nuclei,” 1997.
- [79] A. Kårnsås, A. L. Dahl, and R. Larsen, “Learning histopathological patterns,” *Journal of pathology informatics*, vol. 2, 2011.

- [80] J. Shi and J. Malik, "Normalized cuts and image segmentation," *IEEE Trans. on Pattern Analysis and Machine Intelligence (TPAMI)*, vol. 22, no. 8, pp. 888–905, 2000.
- [81] H. Chang, J. Han, A. Borowsky, L. Loss, J. W. Gray, P. T. Spellman, and B. Parvin, "Invariant delineation of nuclear architecture in glioblastoma multiforme for clinical and molecular association," *IEEE Transactions on Medical Imaging*, vol. 32, no. 4, pp. 670–682, 2013.
- [82] X. Lou, U. Koethe, J. Wittbrodt, and F. Hamprecht, "Learning to segment dense cell nuclei with shape prior," in *IEEE Conference on Computer Vision and Pattern Recognition (CVPR)*, June 2012, pp. 1012–1018.
- [83] C. Park, J. Z. Huang, J. X. Ji, and Y. Ding, "Segmentation, inference and classification of partially overlapping nanoparticles," *IEEE Transactions on Pattern Analysis and Machine Intelligence (TPAMI)*, vol. 35, no. 3, pp. 669–681, 2013.
- [84] D. C. Cireşan, A. Giusti, L. M. Gambardella, and J. Schmidhuber, "Mitosis detection in breast cancer histology images with deep neural networks," in *Medical Image Computing and Computer-Assisted Intervention–MICCAI 2013*, 2013, pp. 411–418.
- [85] M. Veta, P. J. van Diest, R. Kornegoor, A. Huisman, M. A. Viergever, and J. P. Pluim, "Automatic nuclei segmentation in h&e stained breast cancer histopathology images," *PloS one*, vol. 8, no. 7, p. e70221, 2013.
- [86] S. Kothari, Q. Chaudry, and M. Wang, "Automated cell counting and cluster segmentation using concavity detection and ellipse fitting techniques," in *Proc. of IEEE Inter. Symposium on Biomedical Imaging (ISBI)*, 28 2009–july 1 2009, pp. 795–798.
- [87] H. Su, F. Xing, J. Lee, C. Peterson, and L. Yang, "Automatic myonuclear detection in isolated single muscle fibers using robust ellipse fitting and sparse optimization," *IEEE/ACM Trans. on Computational Biology and Bioinformatics*, vol. PP, no. 99, pp. 1–1, 2013.
- [88] J. Wright, A. Y. Yang, A. Ganesh, S. S. Sastry, and Y. Ma, "Robust face recognition via sparse representation," *IEEE Transactions on Pattern Analysis and Machine Intelligence (TPAMI)*, vol. 31, no. 2, pp. 210–227, 2009.
- [89] H. Chang, Y. Zhou, P. Spellman, and B. Parvin, "Stacked predictive sparse coding for classification of distinct regions in tumor histopathology," in *IEEE International Conference on Computer Vision (ICCV)*, 2013, pp. 169–176.
- [90] S. Liao, Y. Gao, and D. Shen, "Sparse patch based prostate segmentation in ct images," in *Medical Image Computing and Computer-Assisted Intervention–MICCAI 2012*. Springer, 2012, pp. 385–392.
- [91] S. Zhang, X. Li, J. Lv, X. Jiang, D. Zhu, H. Chen, T. Zhang, L. Guo, and T. Liu, "Sparse representation of higher-order functional interaction patterns in task-based fmri data," in *Medical Image Computing and Computer-Assisted Intervention–MICCAI 2013*. Springer, 2013, pp. 626–634.
- [92] F. Xing and L. Yang, "Robust selection-based sparse shape model for lung cancer image segmentation," in *Medical Image Computing and Computer-Assisted Intervention (MICCAI)*, 2013, pp. 404–412.

- [93] K. Yu, T. Zhang, and Y. Gong, “Nonlinear learning using local coordinate coding.” in *NIPS*, vol. 9, 2009, p. 1.
- [94] Y. Huang, Z. Wu, L. Wang, and T. Tan, “Feature coding in image classification: A comprehensive study,” 2013.
- [95] H. J. Seo and P. Milanfar, “Training-free, generic object detection using locally adaptive regression kernels,” *IEEE Transactions on Pattern Analysis and Machine Intelligence (TPAMI)*, vol. 32, no. 9, pp. 1688–1704, 2010.
- [96] M. Aharon, M. Elad, and A. Bruckstein, “SVD: An algorithm for designing over-complete dictionaries for sparse representation,” *IEEE Transactions on Signal Processing*, vol. 54, no. 11, pp. 4311–4322, 2006.
- [97] J. W. Schneider and P. Borlund, “Matrix comparison, part 1: Motivation and important issues for measuring the resemblance between proximity measures or ordination results,” *Journal of the American Society for Information Science and Technology*, vol. 58, no. 11, pp. 1586–1595, 2007.
- [98] H. Takeda, S. Farsiu, and P. Milanfar, “Kernel regression for image processing and reconstruction,” *IEEE Transactions on Image Processing (TIP)*, vol. 16, no. 2, pp. 349–366, 2007.
- [99] D. Comaniciu, V. Ramesh, and P. Meer, “Kernel-based object tracking,” *IEEE Transactions on Pattern Analysis and Machine Intelligence (TPAMI)*, vol. 25, no. 5, pp. 564–577, 2003.
- [100] Q. Yu, T. B. Dinh, and G. Medioni, “Online tracking and reacquisition using co-trained generative and discriminative trackers,” in *Proc. of European Conf. on Computer Vision (ECCV)*, 2008, pp. 678–691.
- [101] X. Mei and H. Ling, “Robust visual tracking and vehicle classification via sparse representation,” *IEEE Trans. on Pattern Analysis and Machine Intelligence (TPAMI)*, vol. 33, no. 11, pp. 2259–2272, 2011.
- [102] P. Perona and J. Malik, “Scale-space and edge detection using anisotropic diffusion,” *IEEE Trans. on Pattern Analysis and Machine Intelligence (TPAMI)*, vol. 12, no. 7, pp. 629–639, 1990.

## Vita

### 1. Background:

- Name: Hai Su
- Place of Birth: Pengshan, Sichuan, China

### 2. Academic Degrees:

- Bachelor of Engineering in Electrical Engineering: University of Electronic Science and Technology of China, Sichuan, China, 2003.
- Master of Engineering in Biomedical Engineering: University of Electronic Science and Technology of China, Sichuan, China, 2003.

### 3. Professional Experience

- Research and Development Engineer, Huawei Technology, Inc, 2006-2007
- Teaching Assistant, Illinois Institute of Technology, 2009-2011
- Research Assistant, University of Kentucky, 2011-2014

### 4. Publications

- Hai Su, Fuyong Xing, Jonah D. Lee, Charlotte A. Peterson, Lin Yang: Automatic Myonuclear Detection in Isolated Single Muscle Fibers Using Robust EllipseFitting and Sparse Representation. IEEE/ACM Trans. Comput. Biology Bioinform. 11(4): 714-726 (2014)
- Hai Su, Fuyong Xing, Jonah D. Lee, Charlotte A. Peterson, Lin Yang: Learning based automatic detection of myonuclei in isolated single skeletal muscle fibers using multi-focus image fusion. ISBI 2013: 432-435
- Fuyong Xing, Hai Su, Lin Yang: An Integrated Framework for Automatic Ki-67 Scoring in Pancreatic Neuroendocrine Tumor. MICCAI (1) 2013: 436-443